Attractors for the motion of a finite-size particle in a two-sided lid-driven cavity

Haotian Wu[1], Francesco Romanò[1,2] and Hendrik C. Kuhlmann[1],†

[1]Institute of Fluid Mechanics and Heat Transfer, TU Wien, Getreidemarkt 9, 1060 Vienna, Austria

[2]Univ. Lille, CNRS, ONERA, Arts et Métiers Institute of Technology, Centrale Lille, UMR 9014 – LMFL – Laboratoire de Mécanique des Fluides de Lille – Kampé de Fériet, F-59000, Lille, France

The motion of a single spherical particle in a two-sided lid-driven cavity is investigated experimentally. The flow in which the particle moves is created by two facing cavity sidewalls which move with equal velocity in opposite directions. For a long cavity with width-to-height cross-sectional aspect ratio $\Gamma = W/H = 1.6$ the flow field at Reynolds number $Re = 400$ consists of steady spatially periodic three-dimensional convection cells. Nearly neutrally buoyant particles with radius in units of H ranging from 1.1×10^{-2} to 7.1×10^{-2} are found to be attracted to periodic or quasi-periodic orbits in close vicinity of Kolmogorov–Arnold–Moser (KAM) tori of the unperturbed flow. Like the KAM tori the attractors of neutrally buoyant particles arise in mirror-symmetric pairs within each convection cell. The particle attractors are created by a dissipative effect in the dynamical system describing the particle motion which arises when the finite-size particle closely passes the moving walls. When the particle density deviates from that of the fluid, inertial attractors arise whose symmetry is broken by buoyancy, and other periodic attractors are created which do not have KAM tori as counterparts.

Key words: chaotic advection, particle/fluid flow

1. Introduction

Particle-laden flows arise in many bounded flows of small characteristic length scale. Examples are biomedical applications (Dong, Inthavong & Tu 2017), particle sorting in micro-channels (Matsunaga *et al.* 2017) and quantum super-fluidics (La Mantia 2017). Often, the volume fraction of the particulate phase is very small and the particle size is very small compared to the size of the flow domain. Under these conditions particle–particle and particle–wall interactions are very rare and the motion of an individual spherical particle can be well described by the Maxey–Riley equation (Maxey & Riley 1983) for the centroid of the particle, provided the particle Reynolds and the particle Stokes numbers are small and the particle moves at a distance from the boundary which is large compared to the particle size. In this frequently employed theoretical model

† Email address for correspondence: hendrik.kuhlmann@tuwien.ac.at

a major simplification of the general two-phase problem results from the approximation of the flow field being unaffected by the presence of the particles (one-way coupling) and the particle motion being approximated by an ordinary differential equation.

If, however, a particle moves at a distance from the wall which is no longer large compared to the particle size, the Maxey–Riley equation breaks down. Although a number of asymptotic solutions exist for certain configurations when a sphere moves close to a boundary (Jeffery 1915; Brenner 1961; Chaoui & Feuillebois 2003), there exists no universally valid extension of the Maxey–Riley model which would allow an accurate description of the motion of a spherical particle in the full domain up to the walls.

The breakdown of the Maxey–Riley model is frequently met for particles suspended in millimetric thermocapillary flows (Schwabe *et al.* 2007; Romanò & Kuhlmann 2019), in micro-flows (Wang, Jalikop & Hilgenfeldt 2011; Karimi, Yazdi & Ardekani 2013) or even in nano-flows (Orlishausen *et al.* 2017), because the particle size relative to the domain size can be much larger than, e.g. 0.1 %. While fully resolving simulations of the fully coupled two-phase problem is computationally very expensive, attempts have been made to treat the near-wall motion of a particle or the particle–particle interaction supplementing the Maxey–Riley equation with force models (Breugem 2010; Romanò, Kunchi Kannan & Kuhlmann 2019*a*) based on asymptotic solutions, e.g. by Brenner (1961), dedicated numerical fits (Romanò, des Boscs & Kuhlmann 2020) or by an inelastic collision (Hofmann & Kuhlmann 2011).

The lack of a Maxey–Riley-like model to describe the particle motion in the full domain accessible to the particle is an open problem in micro-flows. In particular, technical applications requiring particle selection or sorting involve the motion of particles near boundaries in a distance much smaller than the particle size (Wang *et al.* 2012). An example is the separation of blood cells from the plasma (Toner & Irimia 2005). Alongside with the importance of the flow boundaries on the particle motion, the fluid flow in small-length-scale systems tends to be laminar, and is often three-dimensional and quasi-steady.

Particles suspended in small-length-scale incompressible three-dimensional steady flows can be attracted to particular orbits leading to a partial or nearly complete de-mixing of the suspension. A paradigm for the boundary effect on the particle motion is the flow in a thermocapillary liquid bridge in which many particles of suitable size can be rapidly attracted to periodic particle accumulation structures (PAS) (Tanaka *et al.* 2006). The fact that the de-mixing is most rapid for particles density matched to the liquid and depends on the particle size (Schwabe *et al.* 2007) is a clear indicator for the role of the boundary effect on the motion of a finite-size particle. This effect was elaborated within a minimum model by Hofmann & Kuhlmann (2011), based on advection in the bulk and an inelastic collision of the particle with the free surface of the liquid bridge. Depending on the particle size they predicted the existence of periodic and quasi-periodic attractors which are located on Kolmogorov-Arnold-Moser (KAM) tori (Aref 1984; Ottino 1989) of the underlying three-dimensional incompressible flow. A review was given by Romanò & Kuhlmann (2019). Since this type of particle clustering is solely due to the particle size, Romanò, Wu & Kuhlmann (2019*b*) coined the term finite-size coherent structures (FSCS) for these attractors to distinguish them from the well-known Lagrangian coherent structures (LCS) which are caused by inertia (Haller 2015). Typically, FSCS form much more rapidly than inertial LCS, because the attraction rate to FSCS scales with the Reynolds number of the flow (Kuhlmann *et al.* 2014; Muldoon & Kuhlmann 2016; Romanò *et al.* 2019*a*), while the inertial attraction rate (inverse inertial time) is very small for small and nearly neutrally buoyant particles.

Despite the many attractors (LCS, FSCS) for the particle motion found and characterised, little experimental work has been carried out to prove their existence, to test their robustness and to quantify their spatio-temporal properties. The current investigation is intended to rigorously analyse the behaviour of particles in a non-trivial steady three-dimensional incompressible flow. In order to isolate the particle–boundary effect on the particle trajectories and on the particle attractors we consider particles whose density is most accurately matched to that of the fluid. By controlling small deviations from the density-matching limit we carve out the effect of inertia and buoyancy which are found to break certain symmetries of the particle motion attractors created by the boundary effect. Quantitative information about the particle dynamics is provided alongside with Poincaré sections and spectra. These data should help understand the complex dynamics found and may serve as reference for the development of better theoretical models (see e.g. Cui *et al.* 2020) to describe the wall effect on the particle motion.

To that end we apply long-term particle tracking to reconstruct the trajectories of spherical particles suspended in the flow in a long cuboidal cavity which is driven by the anti-parallel motion of two facing walls (Kuhlmann, Wanschura & Rath 1997). The flow system was selected, because a steady three-dimensional flow robustly arises at relatively low Reynolds numbers in the range of approximately $\Gamma \approx 1.2$–1.8. (Albensoeder & Kuhlmann 2002; Blohm & Kuhlmann 2002). For supercritical Reynolds numbers Romanò, Albensoeder & Kuhlmann (2017) have thoroughly investigated the flow topology for $\Gamma = 1.7$ and found coexisting regular (KAM tori) and chaotic streamlines which form the template on which FSCS are based. The existence of attractors in this type of system has been predicted Kuhlmann *et al.* (2016) and confirmed experimentally by Wu, Romanò & Kuhlmann (2017) and Romanò *et al.* (2019*b*). Here, we systematically investigate the attractors and establish accurate quantitative data on their existence range and their properties which should aid the development of improved particle–boundary interaction models like, e.g. those employed by Breugem (2010) and Romanò *et al.* (2019*a*).

Section 2 describes the experimental set-up and the particle tracking. In § 3 the properties of the cavity flow under consideration are discussed together with the numerically computed topology of the flow and its consequences for the particle motion. This is followed, in § 4, by a presentation of the experimental results for the motion of almost density-matched particles and the dependence of the attractors on the particle size. In § 5 the motion of particles is measured for which inertia and buoyancy are gaining importance. Finally, the results are discussed in the context of theoretical and numerical modelling and conclusions are drawn in § 6.

2. Experimental methods

2.1. *Experimental apparatus*

We consider the motion of a single spherical particle in a nearly cuboidal, two-sided lid-driven cavity. For the experiments we use the apparatus of Siegmann-Hegerfeld, Albensoeder & Kuhlmann (2008, 2013) who studied the hydrodynamic instability of the nominally two-dimensional vortex flow in this system. The cavity is shown schematically in figure 1 (dashed lines). The fluid motion in the cavity is driven by two rotating cylinders (grey) made from stainless steel which confine the cavity laterally in x direction. In the positive vertical (y) and in the second horizontal direction (z), the cavity is bounded from the top and from the sides by transparent plane Plexiglas walls which allow for an optical access to the interior of the cavity. The bottom of the cavity is made from black Polymethyl methacrylate (PMMA) to minimise undesired optical reflections and to

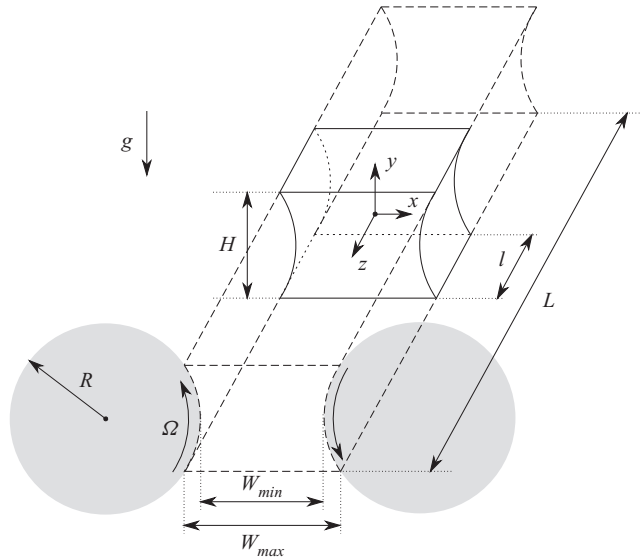*H. Wu, F. Romanò and H. C. Kuhlmann*

FIGURE 1. Sketch of the cavity (dashed lines) within which the fluid motion is induced by tangentially moving sidewalls realised by rotating cylinders. Their cross-sections are shown in grey and their rotation direction is indicated by arrows. The size of the cylinders relative to the cavity has been reduced in the drawing. The full lines delineate a typical periodic convection cell which exists in the supercritical flow.

improve the contrast between the white suspended particle and the background when the particle is observed from above. Since the radius of the rotating cylinders (not drawn to scale in figure 1) is large compared to the gap between the cylinders and the height of the cavity, deviations from a rectangular cuboidal shape are moderate, but not negligible as will be explained later.

Both rotating cylinders have a radius of $R = 135$ mm. The height of the cavity in y direction is $H = 40.1$ mm and the minimum and maximum widths (in x direction) between the two moving cylinders are, respectively, $W_{min} = 62.9$ mm and $W_{max} = 65.9$ mm. The arithmetic mean value $\bar{W} = 64.4$ mm is used to define the aspect ratio $\Gamma = \bar{W}/H = 1.6$ (rounded). The rotating cylinders, the cavity bottom, and the transparent top and end walls are mounted in a larger container (not shown in figure 1) which is also filled with the working liquid. The container serves the purpose to thermalise the cavity and to compensate for a minute exchange of liquid through the small gaps between the moving cylinders and the stationary walls. All walls have been carefully adjusted to minimise the exchange of liquid between the cavity and the surrounding reservoir.

Silicone oil (Bayer Baysilone fluid M20) with nominal kinematic viscosity $\nu = 20$ cSt and density $\rho_f = 0.95$ g cm^{-3} at $T = 25\,°$C is used as the working fluid. The viscosity of the fluid has been measured independently to establish a gauge function $\nu(T)$, and it is shown in figure 2 together with the density of the liquid. Both cylinders rotate with the same angular velocity Ω and in the same sense to create an opposing motion of the lateral cavity walls. The Reynolds numbers associated with the rotating cylinders (subscripts 1 and 2)

$$Re = Re_1 = Re_2 = \frac{\Omega R H}{\nu(T)}, \qquad (2.1)$$
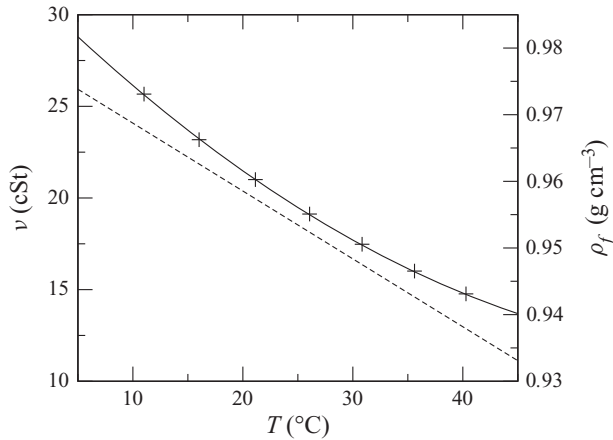
FIGURE 2. Kinematic viscosity (pluses) measured by a Cannon-Fenske capillary flow viscometer and polynomial fit $\nu = a_0 + a_1T + a_2T^2$ (full line) with $a_0 = 31.6717$, $a_1 = -0.5976$ and $a_2 = 0.0044$, where ν and T are measured in cSt and °C, respectively. The density ρ_f (dash line) is a linear fit of the data provided by the manufacturer.

are kept constant by keeping the temperature T constant during each experiment. The temperature of the liquid is controlled with an accuracy of ± 0.1 °C by circulating fluid from the outer bath through a thermostat (Haake F6). Owing to the high thermal conductivity of the steel cylinders and the slow temperature variation, the system can be considered in thermal equilibrium. Estimating all tolerances, the Reynolds number can be controlled with an accuracy of 0.5 %.

For an infinitely long cavity and aspect ratio $\Gamma = 1.6$ the low-Reynolds-number flow would be two-dimensional. Theoretically, this basic flow becomes unstable due to the elliptic instability at a relatively low Reynolds number $Re_c \approx 200$ (Albensoeder & Kuhlmann 2002) and gives way to steady periodic convection cells of width l (full lines in figure 1), corresponding to half a wavelength in the z direction. At criticality $l/H = \lambda/2 \approx 1.35$, where λ is the non-dimensional wavelength. The long spanwise length in the experiment of $L = 435$ mm, corresponding to a span aspect ratio $\Lambda = 10.85$, permits us to create a nearly two-dimensional basic flow and a nearly spanwise-periodic supercritical flow in most parts of the cavity, except near the end walls (cf. Siegmann-Hegerfeld *et al.* 2013).

In each experiment, the fluid is seeded with a single spherical particle made from polyethylene. Different particles are used with particle radius a_p ranging from 0.15 to 2.85 mm and particle-to-fluid density ratios $\varrho = \rho_p/\rho_f$ ranging from 0.94 to 1.08. The particle-to-fluid density ratio ϱ was determined by measuring the Stokes settling velocity in a separate well-controlled experiment. Table 1 lists the particle sizes, their relative densities ϱ, corresponding uncertainties $\Delta\varrho$ at the operating temperature, Stokes number in viscous scaling $St = 2a^2/9$ and Stokes number in convective scaling $St_{conv} = Re\,St$. Since the temperature of the liquid in the cavity is controlled up to ± 0.1 °C, the tolerances for the density ratio determined by Stokes settling (table 1) is increased to $\Delta\varrho \approx \pm 0.00006$ in the actual experiment due to fluctuations of the liquid density.

2.2. *Particle tracking*

The trajectory $X(t)$ of the centroid of the particle is obtained by recording its motion by two synchronised cameras (type: FLIR GS3-U3-32S4M-C) equipped with lenses of

a_p [mm]	a	T [°C]	ϱ	$\Delta\varrho$	St	St_{conv}
0.15	0.004	26.7	1.003	±0.0005	3.56×10^{-6}	1.42×10^{-3}
0.45	0.011	23.7	1.0001	±0.00001	2.69×10^{-5}	1.08×10^{-2}
0.48	0.012	23.7	1.045	±0.003	3.20×10^{-5}	1.28×10^{-2}
0.48	0.012	26.4	1.08	±0.006	3.20×10^{-5}	1.28×10^{-2}
0.50	0.012	25.5	0.94	±0.005	3.20×10^{-5}	1.28×10^{-2}
0.50	0.012	26.0	1.023	±0.001	3.20×10^{-5}	1.28×10^{-2}
0.53	0.013	24.5	1.06	±0.005	3.76×10^{-5}	1.50×10^{-2}
1.00	0.025	23.7	1.0001	±0.00001	1.39×10^{-4}	5.56×10^{-2}
1.58	0.039	26.1	1.0001	±0.00001	3.38×10^{-4}	1.35×10^{-1}
1.58	0.039	25.0	1.001	±0.0001	3.38×10^{-4}	1.35×10^{-1}
1.58	0.039	28.0	1.006	±0.0003	3.38×10^{-4}	1.35×10^{-1}
2.00	0.050	34.3	1.0001	±0.00001	5.56×10^{-4}	2.22×10^{-1}
2.37	0.059	26.2	1.00005	±0.000007	7.74×10^{-4}	3.09×10^{-1}
2.85	0.071	27.1	1.00007	±0.000011	1.12×10^{-3}	4.48×10^{-1}

TABLE 1. Particle radii a_p, non-dimensional particle radii $a = a_p/H$, operating temperature, particle-to-fluid densities $\varrho = \rho_p/\rho_f$, uncertainties $\Delta\varrho$ obtained from measuring the settling velocity and Stokes number in viscous scaling $St = 2a^2/9$ and in convective scaling $St_{conv} = Re\,St$.

focal length $f_l = 16$ mm. Records from both cameras are taken using aperture $f/4$ and a frame rate of $f = 20$ Hz. The cameras are mounted above the transparent top lid of the cavity and monitor the cavity under different angles (figure 39 in appendix A). Once the positions of the particle images on the sensor planes of the cameras have been determined, the three-dimensional particle position can be reconstructed via ray tracing as described in appendix A. Consecutive positions of the particle yield its trajectory.

In a first step, the centroids of the particle images $\boldsymbol{x}_S^{(i)} = [x_S^{(i)}(t), y_S^{(i)}(t)]$ on each sensor plane (superscript $i = 1, 2$) must be determined. To that end a background image, obtained by averaging 200 frames, is subtracted from each original grey-scale frame. Thereafter, a Laplacian-of-Gaussian (LoG) filter is applied to reduce the noise. The maximum brightness value will arise at the centre of a blob-shaped structure which represents the image of the particle (Szeliski 2010). Since the LoG filter is scale oriented, by selecting different values of the standard deviation σ of the LoG kernel, the response of particles with different sizes is different. This property helps to distinguish particles with different sizes (if used simultaneously) and filter noise due to reflections from small debris particles or air bubbles. Sample images corresponding to each of the above processing steps are shown in figure 3.

After the sensor-based coordinates $\boldsymbol{x}_S^{(1)}$ and $\boldsymbol{x}_S^{(2)}$ have been determined for each frame of the video record, the cavity-centred world coordinates of the trajectory $X_W(t) = [X_W(t), Y_W(t), Z_W(t)]$ are obtained by a ray tracing process (Yamashita, Fujii & Kaneko 2008; Pedersen *et al.* 2018) which is described in detail in appendix A.

The flow at the targeted Reynolds number $Re = 400$ arises in form of $N = 8$ steady convection cells which are numbered consecutively by an index n. Since we are interested in the particle's trajectory relative to the cellular flow, the cavity-centred world coordinates $X_W(t)$ of the trajectory are transformed to the final cell-centred coordinates $X(t)$. Assuming the trajectory remains in the same convection cell n for all time, the cell
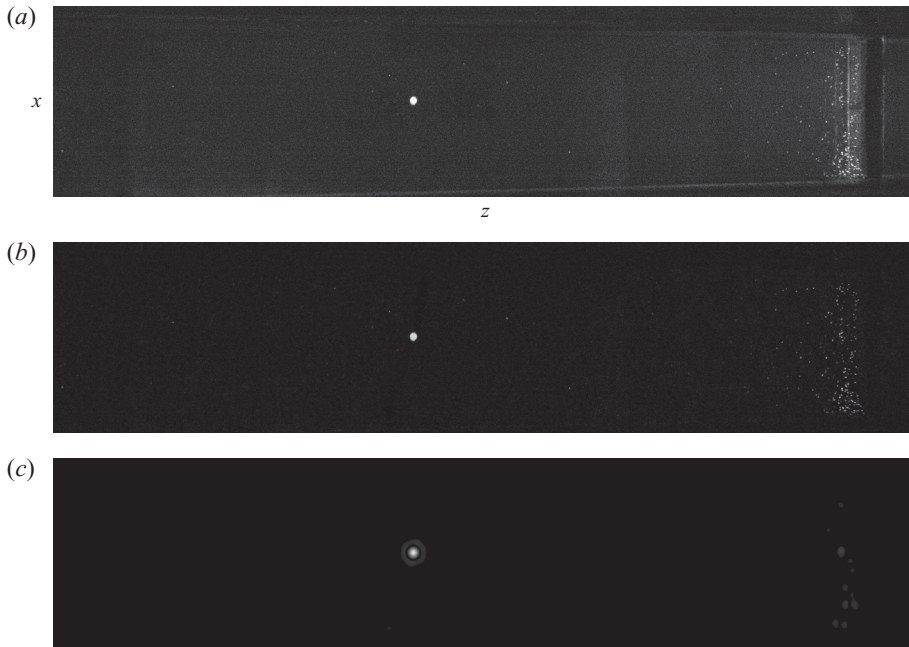
FIGURE 3. Image processing of a single frame: (*a*) original image, (*b*) subtraction of the background image, (*c*) convolution with a LoG filter.

number n relative to the reference cell $n = 0$ is detected by rounding $n = \texttt{round}[(Z_W - \lambda/4)/(\lambda/2)]$. The shift by half a cell width $-\lambda/4$ is applied to the coordinate Z_W, since the origin of the cavity-centred coordinates $(X_W, Y_W, Z_W) = (0, 0, 0)$ lies on the boundary between the two cells nearest to the cavity centre for an even number of cells. The cell-centred coordinates (X, Y, Z) of the trajectory are then obtained as

$$X(t) = X_W(t), \tag{2.2a}$$

$$Y(t) = Y_W(t), \tag{2.2b}$$

$$Z(t) = (-1)^n \left[Z_W(t) - n\frac{\lambda}{2} - \lambda/4 \right]. \tag{2.2c}$$

Hence, the trajectory X_W is mapped to the reference cell $n = 0$ by a shift of $(\lambda/4)(2n + 1)$ in z. The factor $(-1)^n$ causes a reflection with respect to $Z = 0$ if the original cell index n is odd. This is due to the full period of the flow consisting of two cells which are reflection symmetric with respect to their boundaries (Blohm & Kuhlmann 2002; Romanò *et al.* 2017). Since the phase of the cellular flow in the central region of the cavity may slightly vary from one experimental realisation to the other, the Z coordinate is corrected by a tiny additive amount ΔZ_{exp} which is determined using point-cloud matching. Typically, the average shift is $\overline{\Delta Z}_{exp} = 0.01 \ll \lambda/2$ for a series of 20 repeated experiments, with standard deviation $\sigma_{\Delta Z} = 0.01$.

3. Transport of particles

Results are mainly presented in non-dimensional form, scaling all lengths, velocities and time by H, $\nu(T)/H$ and $H^2/\nu(T)$, respectively, where $\nu(T)$ is the viscosity of the fluid
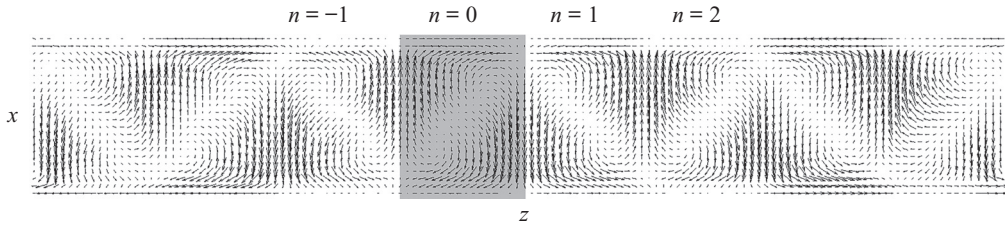
FIGURE 4. Particle image velocimetry (PIV) measurement showing the two-dimensional velocity field $[u(x_W, z_W), w(x_W, z_W)]$ in the horizontal plane $y_W = 0$ for $Re = 400$. The reference cell $n = 0$ is shaded.

in the respective experiment carried out at the temperature T. Exceptions concern the time and frequency which, for convenience, are also given in dimensional form together with the temperature. The coordinate origin is placed in the centre of the reference convection cell (full lines in figure 1). We use non-dimensional cell-centred Cartesian coordinates (x, y, z), flow velocities (u, v, w) and trajectory coordinates $(X, Y, Z)(t)$. In addition to the flow field, the motion of a spherical particle is determined by its density ratio $\varrho = \rho_p/\rho_f$ and its non-dimensional radius $a = a_p/H$. Furthermore, we define a particle Stokes number $St := 2a^2/9$ based on the velocity scale ν/H of the flow.

3.1. *Fluid flow*

3.1.1. *General properties*

Upon an increase of the Reynolds number, the nearly two-dimensional vortex flow in the cavity becomes unstable and a three-dimensional cellular flow is established via a supercritical bifurcation. The theoretical critical data for an infinitely extended cavity $(\Lambda \to \infty)$ with a rectangular cross-section of $\Gamma = 1.5$ are $Re_c = 191.9$ and $\lambda_c = 2.67$ (Albensoeder & Kuhlmann 2002), while the critical data for $\Gamma = 1.7$ are $Re_c = 211.53$ and $\lambda_c = 2.73$ (Romanò *et al.* 2017). Using the current set-up with $\Gamma = 1.6$ and slightly curved moving walls, Siegmann-Hegerfeld (2010) experimentally obtained $Re_c(\Gamma = 1.6) = 205$. This experimental value compares very well with the numerical critical Reynolds number $Re_c(\Gamma = 1.6) = 200$ for a rectangular cross-section, also reported in Siegmann-Hegerfeld (2010).

Using the same viscous scaling (ν, H) and fixing the Reynolds number to $Re = 400$ in the present study, we find the cellular flow to always consist of eight stationary cuboidal convection cells occupying the whole cavity. This corresponds to a mean non-dimensional wavelength $\bar{\lambda} = \Lambda/4 = 2.72$ which is compatible with the previous numerical results for the periodic rectangular cavity (Albensoeder & Kuhlmann 2002; Romanò *et al.* 2017). The velocity field at the midplane $y = 0$ over the full extent of the cavity for $Re = 400$, shown in figure 4, illustrates the cellular flow structure. The rigid end-wall conditions at $z_W = \pm\Lambda/2$ modify the cellular flow mainly within the cells neighbouring the end walls. The four cells (corresponding to two wavelengths) in the central region near $z = 0$ are hardly affected and they are practically periodic in z. This is verified by the velocity profile along the centre line $(x, y) = (0, 0)$ of the cavity shown in figure 5. The cell boundaries are characterised by planes of constant z on which the spanwise velocity $w = 0$ vanishes. Furthermore, the flow is reflection symmetric with respect to each cell boundary, and it is point symmetric with respect to the cell centre within each convection cell (Blohm & Kuhlmann 2002; Romanò *et al.* 2017). For a more comprehensive review on hydrodynamic instabilities in lid-driven cavities we refer to Kuhlmann & Romanò (2019).
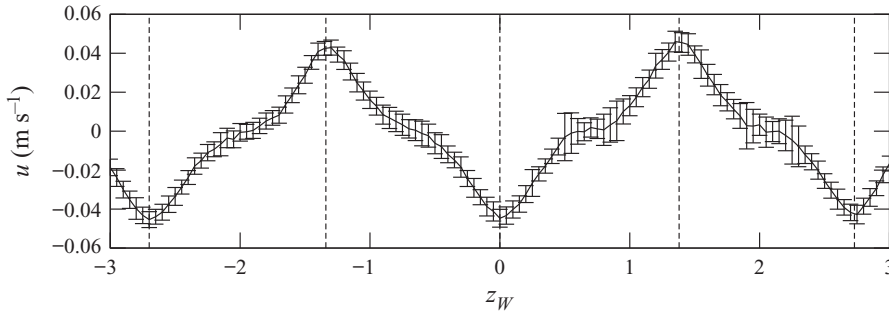
FIGURE 5. Laser-Doppler-velocimetry measurement of the dimensional velocity component $u(z_W)$ along cavity centreline $(x_W, y_W) = (0, 0)$ for $Re = 400$ as function of z_W (dimensionless). The cell boundaries, indicated by vertical dashed lines, coincide with the extrema of $u(z_W)$.

3.1.2. *Numerical flow topology*

The structure of the streamlines is of key importance for understanding the motion of nearly neutrally buoyant finite-size particles in the system under consideration (Kuhlmann *et al.* 2016; Romanò *et al.* 2017). Therefore, the flow field is numerically calculated, taking into account the curvature of the moving walls and using a spectral-element method employing high-order Lagrange polynomials. The discretisation of the velocity field is based on Gauss–Legendre–Lobatto nodes defining the Lagrange polynomials in the function space $\mathbb{P}_N$. For the pressure, Gauss–Legendre nodes are employed with corresponding Lagrange polynomials in $\mathbb{P}_{N-2}$. The temporal integration is carried out implementing the high-order stiffly stable scheme of Karniadakis, Israeli & Orszag (1991) by using third-order backward differentiation formulae for the linear terms of the Navier–Stokes equation and third-order explicit integration schemes for the nonlinear convective terms. The open-source solver NEK5000 (Fischer, Lottes & Kerkemeier 2008) is used to carry out the numerical simulations distributing 20 elements along each space direction of one period of the flow and using eighth-order polynomials for the velocity field. Since the Galerkin weak formulation is used for the discretisation, an over-integration method which employs 12^3 Gaussian nodes per element is used to eliminate aliasing errors.

No-slip and no-penetration boundary conditions are imposed along the walls. In the z direction periodic boundary conditions with $\lambda = 2.618$ have been used in the simulations. To reduce the singularity due to the discontinuous boundary conditions along the straight edges between the stationary and the moving walls the three spectral components of the velocity field with the highest frequency are filtered within the elements next to the singular corner. The time-dependent flow field is considered to have become stationary once the convergence criterion (in viscous scaling)

$$\max_{\boldsymbol{x}, i} \frac{|u_i(\boldsymbol{x}, t) - u_i(\boldsymbol{x}, t - \Delta t)|}{\Delta t} \leq 10^{-7}, \tag{3.1}$$

is satisfied, where Δt is the time step.

The algorithm of Romanò *et al.* (2017) is used to integrate streamlines of the steady flow. For $Re = 400$ chaotic and regular streamlines coexist, similar as in the strictly rectangular cavity ($\Gamma = 1.7$, Romanò *et al.* 2017). However, the size, location, and structure of the KAM tori are different due to the curvature of the moving walls. For the present system with curved moving walls we have reconstructed the KAM tori at $Re = 400$ in the same
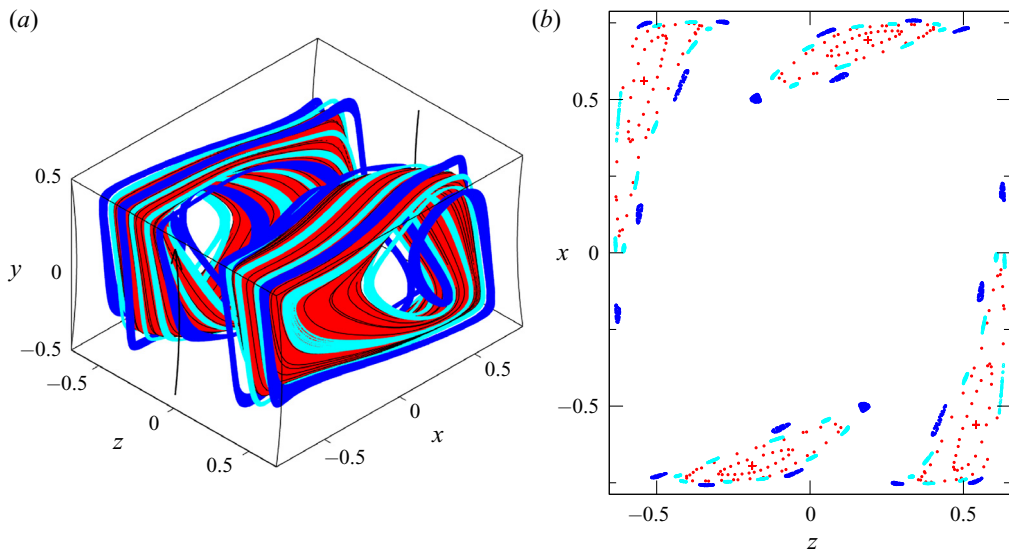
(*a*) (*b*)

FIGURE 6. Numerically calculated KAM tori in the two-sided lid-driven cavity for $Re = 400$ and $\lambda = 2.618$. (*a*) Largest reconstructible KAM tori in a convective cell. The wall motion is indicated by black arrows. (*b*) Poincaré section on $y = 0$ of quasi-periodic streamlines on the KAM tori shown in (*a*). The panel shows the full cross-section of the cell. Poincaré points due to the closed streamlines inside the two main sets of KAM tori with period one are indicated by red pluses. In the Poincaré section the top and bottom left sets belong to the same KAM tori. The top and bottom right sets belong to the point-symmetrically located set of KAM tori.

way as in Romanò *et al.* (2017), Romanò, Hajisharifi & Kuhlmann (2017) and Romanò, Türkbay & Kuhlmann (2020). Owing to the point symmetry of the flow in a single cell, all KAM tori arise as two point-symmetric sets of tori. The resulting largest reconstructible KAM tori are shown in figure 6(*a*) for the generic convection cell (shaded in figure 4). There exist two primary closed streamlines which are surrounded by large KAM tubes (red in figure 6*a*). The cross-sections of these two major KAM tubes are outlined by red dots in figure 6(*b*) which shows a Poincaré section at $y = 0$. The major (red) KAM tubes are surrounded by chaotic streamlines in which higher-order KAM tori are embedded. From figure 6(*b*) it is seen that the primary KAM tubes (red) are surrounded by a set of KAM tori due to a 9 : 1 resonance (cyan) which winds nine times about the primary system of KAM tori. Further away, another set of KAM tori (blue) is found which is caused by a 5 : 1 resonance, winding five times about the red KAM tori. Up to the limits imposed by the resolution and the procedure for detecting KAM tori numerically (Romanò *et al.* 2017) the empty space outside of the tori in figure 6(*a*,*b*) is occupied by chaotic streamlines. Inside of each set of KAM tori a closed streamline exists, which has period 1 (red pluses), 9 (cyan) or 5 (blue).

Properties of a set of KAM tori relevant for the particle motion are the distances Δ_ψ of the closed streamline and Δ_T of the largest reconstructible KAM torus from the boundaries, in particular from the moving walls, and the orbit time τ_{num} of the closed streamline (Mukin & Kuhlmann 2013; Romanò *et al.* 2017, 2019*b*). These characteristic parameters are gathered in table 2 for the three KAM tori near $z = -\lambda/4$ (left side in figure 6*b*).

KAM	τ_{num}	$\Delta_\psi^{y=0.5}$	$\Delta_\psi^{y=-0.5}$	$\Delta_\psi^{x=-\Gamma/2}$	$\Delta_\psi^{x=\Gamma/2}$	$\Delta_T^{y=0.5}$	$\Delta_T^{y=-0.5}$	$\Delta_T^{x=-\Gamma/2}$	$\Delta_T^{x=\Gamma/2}$
Period 1	0.03126	0.098	0.116	0.077	0.076	0.053	0.065	0.037	0.031
Period 5	0.15442	0.050	0.048	0.025	0.028	0.046	0.045	0.024	0.027
Period 9	0.28772	0.049	0.062	0.035	0.027	0.048	0.061	0.034	0.027

TABLE 2. Numerically computed properties of the three different sets of KAM tori for $Re = 400$ and $\lambda = 2.618$ which are located near the cell boundary at $z = -\lambda/4$ (cf. figure 6). Specified are the period τ_{num} of the closed streamline, its closest distance to the boundaries (Δ_ψ) and the closest distances to the boundaries of the largest reconstructible KAM torus (Δ_T) of each set. The superscript indicates the boundary the distance refers to. The distances from the moving walls at $x = \pm\Gamma/2$ were evaluated in x (for constant y); but up to the accuracy given these distances are equal to the wall-normal distances. For the distances of the tori near $z = \lambda/4$ the coordinates in the superscripts need to be multiplied by (-1) (point symmetry).

While the flow topology has been computed for $\lambda = 2.618$, the wavelength in the centre of the cavity was experimentally found to be $\lambda_{exp} \approx 2.7$, as expected from the linear stability analyses (Albensoeder & Kuhlmann 2002; Romanò *et al.* 2017). Nevertheless, flow properties deduced from the numerical simulation with $\lambda = 2.618$ will be compared with experimental results, because tests have shown the difference is very small. For instance, the distance between the intersection points of the closed streamlines of period 1 with the plane $y = 0$ obtained numerically for $\lambda = 2.618$ and for $\lambda = 2.7$ is less than 0.01.

3.2. *Particle motion*

Small, but finite-size, nearly density-matched spherical particles almost move like the fluid. The advection of fluid elements in a steady, three-dimensional incompressible flow represents a locally Hamiltonian system (Bajer 1994), leading to a KAM structure of the streamlines. This property carries over to perfectly advected particles. However, small deviations from advection exist which are caused by the density mismatch between particles and fluid and by the finite size of the particles. Such small deviations from the Hamiltonian dynamics of advected particles are typically dissipative. Due to the dissipation introduced by the particle's finite size and density mismatch in the dynamical system governing its motion, elliptic orbits (such as the closed streamlines of the flow) become stable or unstable limit cycles of the particle motion (Mukin & Kuhlmann 2013; Romanò & Kuhlmann 2018).

To isolate the effect of the particle size on its motion it is useful to eliminate the influence of inertia. Therefore, we shall primarily consider particles whose density mismatch with respect to the fluid has been minimised. For the motion of finite-size density-matched particles Hofmann & Kuhlmann (2011) suggested that attractors for the particle motion can be created by the steric boundary effect if an elliptic orbit of the fluid motion (a closed streamline), surrounded by KAM tori, exists which locally approaches the boundary up to a distance compatible with the particle size, i.e. with the range of boundary-induced forces on the particle. Hofmann & Kuhlmann (2011) and others (see e.g. Mukin & Kuhlmann 2013; Muldoon & Kuhlmann 2013; Romanò & Kuhlmann 2015, 2017*a*; Romanò & Kuhlmann 2018) modelled the particle–boundary interaction by an *ad hoc* one-parameter repulsive inelastic collision. Further refinements aiming at a more realistic modelling are due to Romanò *et al.* (2019*a*,*b*). Independent of the specific theoretical and numerical modelling of the wall effect, the attractors for finite-size

density-matched particles are created by the dissipation the particle experiences during its motion near the boundary: while the particle essentially moves like a fluid element in the bulk either on a chaotic or a regular streamline, it is displaced from its original streamline during its motion near the boundary. Romanò *et al.* (2019*a*) have explained that this effect is generic and termed the resulting coherent structures forming in dilute suspensions finite-size coherent structures.

To carry out experiments which meet the above theoretical conditions for finite-size coherent structures, we first consider the motion of single particles of different sizes for which the density mismatch relative to the fluid is minimised. Thereafter, the effect of the density mismatch is investigated. To minimise effects on the particle motion caused by the end walls at $z_W = \pm \Lambda/2$ only particle trajectories are taken into account which were measured within the four inner convection cells near $z_W = 0$, i.e. for cell indices $n = -1$, 0, 1 and 2 (figure 4).

4. Nearly neutrally buoyant particles

To minimise buoyancy and inertia due to the relative density deviation $\varrho - 1$ between the particle and the fluid, the temperature of the liquid was adjusted as to keep a selected particle floating in quiescent liquid as long as possible. The residual density mismatch was then determined by the sedimentation time using Stokes' formula. This way the density mismatch could be reduced to $|\varrho - 1| \leq 10^{-4}$. If not mentioned otherwise, the density ratio was $\rho = 1.0001$ throughout in this section. Under these conditions and with particle radii in the range $a = O(\Delta_\psi^{x=-\Gamma/2})$ (table 2) the above mechanism of particle–boundary interaction is expected to be the dominant source of dissipation in the dynamical system governing the particle motion.

In the experiments a selected single particle was placed in the cavity. Then the Reynolds number was rapidly increased to $Re = 1600$ and kept constant for at least 60 s. At this Reynolds number the flow is time dependent and fully chaotic. This initial phase of the experiment serves the purpose to assign the particle a random initial condition. After randomisation, the Reynolds number is linearly ramped down to $Re = 400$ with a rate $\Delta Re/\Delta t = 1000$ s^{-1}. The time at which $Re = 400$ is reached defines $t = 0$. For $t > 0$ the Reynolds number is kept constant at $Re = 400$.

Figure 7 shows the spanwise and streamwise velocity components $w(t)$ and $u(t)$, respectively, measured at the cavity midpoint $(x_W, y_W, z_W) = (0, 0, 0)$. In addition, $Re(t)$ is indicated by a dashed line in figure 7(*a*). As can be seen the large-amplitude chaotic flow oscillations of $w(t)$ decay rapidly after ramping down commences at $t = -1.2$ s. At $t = 5$ s after the Reynolds number has reached $Re = 400$ convective cells have already formed, indicated by the vanishing spanwise velocity component $w(t)$ characteristic of a cell boundary. However, the streamwise velocity component $u(t)$, which has a local maximum as a function of z on the cell boundary, decays much slower. Figure 7(*b*) indicates an exponential decay of $u(t)$ which becomes indistinguishable from the noise at time $t \approx 50$ s, which is ∼0.6 times the viscous diffusion time $\tau_\nu = H^2/\nu \approx 80$ s.

4.1. *Case a = 0.05*

Using the length scale $H = 40.1$ mm of the flow domain, a particle with radius $a_p = 2.00$ mm has the non-dimensional radius $a = 0.05$. With $\varrho = 1.0001$ this particle is found to be attracted to a limit cycle. Figure 8 shows this limit cycle (red) in the (x, y) plane (figure 8*a*) and in the (x, z) plane (figure 8*b*) using cell-centred coordinates. At $t_1 = 65$ s the particle's motion has already converged to the periodic attractor. The trajectory was
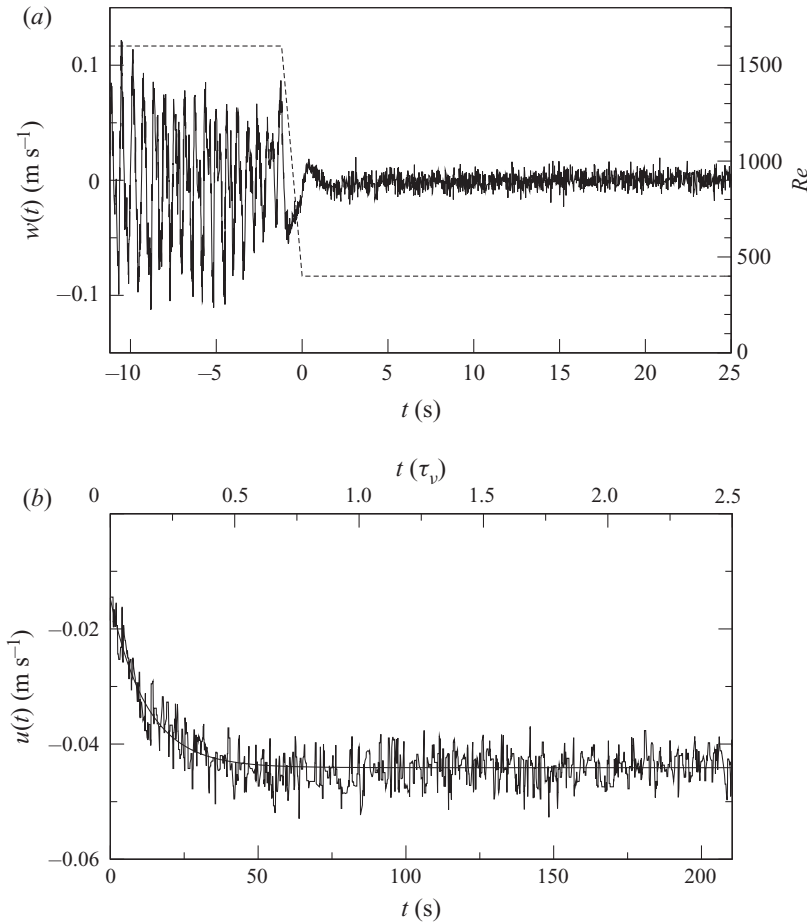
FIGURE 7. Velocity components as functions of time measured by laser Doppler velocimetry (LDV) at the midpoint of the cavity $(x_W, y_W, z_W) = (0, 0, 0)$. At $t \approx -1.2$ s the Reynolds number Re (dashed line in (a)) is ramped down from 1600 and reaches $Re = 400$ at $t = 0$ s. (a) Spanwise velocity component $w(t)$. (b) Streamwise velocity component $u(t)$. The smooth curve in (b) is a fit $u_{fit} = B + Ae^{-t/T_f}$ for $t \in [0, 210.4]$ s with $A = 0.0294$ m s^{-1}, $B = -0.0441$ m s^{-1} and $T_f = 12.2$ s. In addition, the non-dimensional time is shown in units of $\tau_\nu = 84.14$ s. The temperature is $T = 26\,^{\circ}$C.

recorded from t_1 to $t_2 = 115$ s, i.e. for a duration of $t_{rec} = 50$ s. This duration corresponds to 15.5 periods of the limit cycle. It can be seen that the limit cycle closely approaches the boundary of the domain of motion V^* of the particle centroid, which is defined by $V^* = V \backslash P$, where V is the volume occupied by the fluid and P the geometrically prohibited region for the particle centroid, made by a layer of thickness a along all boundaries (indicated by dashed lines for the moving walls only).

The periodicity of the attractor can be verified by the amplitude spectrum (figure 9) of the particle trajectory $X(t) = [X(t), Y(t), Z(t)]$ in cell-centred coordinates, recorded during $[t_1, t_2] = [65, 115]$ s. The amplitude spectra $\hat{X}$ and $\hat{Z}$ of the trajectory only consist of sharp peaks at the fundamental frequency $F_1 = 30.5$ (dimensional frequency $f_1 = 0.31$ Hz) and its harmonics.
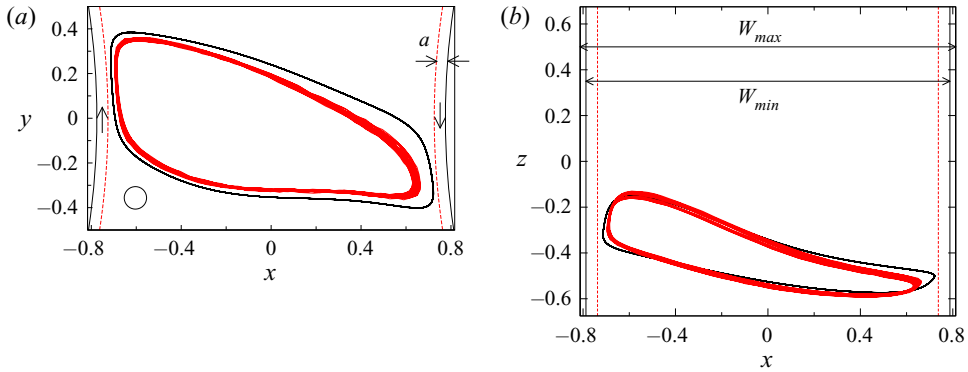
FIGURE 8. Periodic trajectory $X(t)$ (red) of a single particle with $a = 0.05$ ($a_p = 2$ mm) and $\varrho = 1.0001$ shown for $[t_1, t_2] = [65, 115]$ s (≈ 15.5 periods of revolution) in comparison with the numerically computed closed streamline (black) of the main set of KAM tori, corresponding to the two red pluses in figure 6 for $z < 0$. The vertical arrows in (*a*) indicate the direction of motion of the walls. The circle shows the size of the particle. The red dashed lines delineate the layers on the moving walls geometrically inaccessible for the centroid of the particle. The window of z in (*b*) corresponds a full cell width $\lambda/2$. $T = 34.3\,°C$.
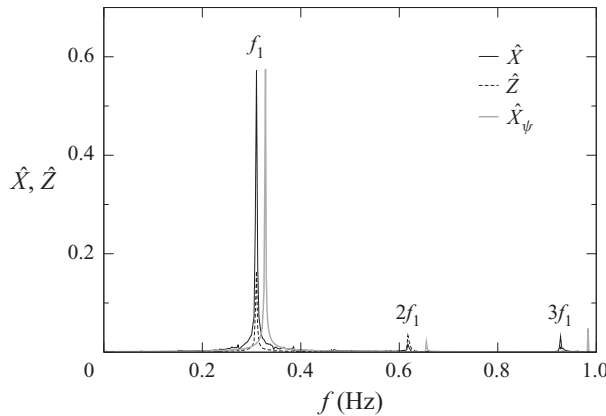
FIGURE 9. Amplitude spectra of the trajectory coordinates $X(t)$ (dashed line) and $Z(t)$ (full line) for a particle with $a = 0.05$ ($a_p = 2.00$ mm) and $\varrho = 1.0001$ moving on the periodic orbit. The fundamental frequency is $F_1 = 30.5$ ($f_1 = 0.31$ Hz); $T = 34.3\,°C$. Also shown is the amplitude spectrum $\hat{X}_\psi$ (grey) of the closed streamline of the period-one set of KAM tori.

The limit cycle in figure 8 (red) forms in the close vicinity of the closed streamline (black) of the period-one set of main KAM tori of the flow, obtained numerically. Also the orbit time $\tau_{exp} = 1/F_1 = 0.0328$ for the period-one limit cycle compares well with the numerical result $\tau_{num} = 0.03126$ (table 2).

The attraction to the limit cycle can be understood in the framework of the mechanism for finite-size coherent structures (Hofmann & Kuhlmann 2011; Romanò et al. 2019b): While the particle nearly follows the flow in the bulk, repeated returns to the moving walls eventually transfer the particle from the chaotic sea to the main KAM torus within which it gets further focussed to the limit cycle. For the present particle size, the limit cycle is created in the vicinity of the closed streamline of the unperturbed flow

(Hofmann & Kuhlmann 2011). As can be seen from figure 8 the particle never collides with the moving walls; there remains a certain small lubrication gap of width δ between the particle's surface and the moving walls. From figure 8 one can also see that the periodic orbit stays much further away from the stationary top and bottom walls, indicating the interaction with the left moving wall at $x < 0$ (closest approach of the attractor to any of the boundaries) provides the main source of dissipation for the dynamic system of the particle motion.

To ensure reproducibility of the result, the experiment has been repeated 36 times. In all cases the particle was attracted to a periodic orbit. However, due to the randomised initial conditions for the particle, the particle could have also been attracted to the other orbit, point-symmetrically located in the same convection cell, because the closed streamlines arise in point-symmetric pairs in each of the convection cells owing to the symmetry of the flow within each cell. Moreover, due to the initial conditions, the particle can be attracted to an orbit near any of the primary closed streamlines in the other convection cells which possess the same KAM structures, or to their mirror-symmetric counterparts. Therefore, in each measurement the particle is found to settle, for $t > 0$, in one of the periodic convection cells. This is demonstrated in figure 10(a) which shows long-exposure photographs of the particle limit cycles (closed wide bright streaks, projection to $y = 0$) for four out of eight cases which are possible within the four innermost convection cells $n = -1, 0, 1, 2$ indicated by vertical dashed lines. Exploiting the symmetries of the flow and of the particle attractors, all periodic attractors can be mapped to any of the two limit cycles existing inside the $n = 0$ reference cell. Figure 10(b) shows the superposition of all 36 single-particle trajectories (red) mapped, using (2.2), to the generic convective cell $n = 0$ in comparison with the closed streamlines (black). The shape and location of the limit cycles compare very well with each other and are located in the very vicinity of one of the two closed streamlines.

Theoretical models typically consider a density-matched particle initially velocity matched to a stationary flow at $t = 0$ (Hofmann & Kuhlmann 2011). If initialised in the chaotic sea, which occupies most of the cavity, the initial part of the particle's trajectory reflects the underlying chaotic streamlines. Once, by way of the particle–boundary interaction, the particle has entered a KAM torus, hosting the attractor, the particle's motion is expected to be nearly regular (for exceptions, see § IV.D.1 of Mukin & Kuhlmann 2013). Therefore, the particle's trajectory should be governed by different time scales during the different phases of its evolution. The first (initial) time scale τ_I is given by the time required for an ensemble of non-interacting particles to be transported near the attractor from their initial conditions at $t = 0$. The second phase of attraction is governed by an oscillatory approach of the particle trajectory to the limit cycle.

In the experimental realisation, however, the particle cannot be introduced velocity matched and its motion is always tied to the fluid motion which is initially transient (figure 7). For that reason, the particle's motion cannot be separated from the relaxation dynamics to the stationary state of the flow. Regardless of this difficulty, we estimate the mean time at which the particle enters the region close to the attractor and its motion becomes non-chaotic. To that end we define the discrete distance from the attractor

$$d_n = \left[(y_n - y^*)^2 + (z_n - z^*)^2 \right]^{1/2}, \tag{4.1a}$$

where $(y_n, z_n) = [y(t_n), z(t_n)]$ is the nth Poincaré point in the plane $x = 0$ at $t = t_n$ and

$$(y^*, z^*) = \frac{1}{K} \sum_{k=N_{max}-K+1}^{N_{max}} (y_k, z_k), \tag{4.1b}$$
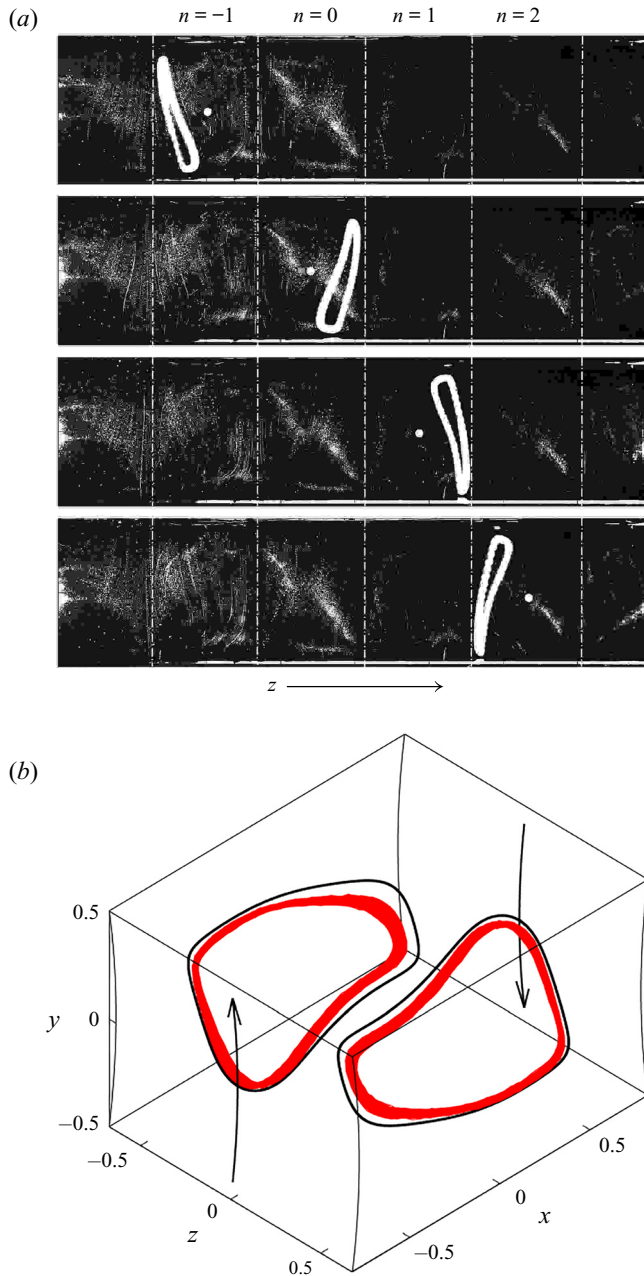
FIGURE 10. (*a*) Long-exposure photographs from the top view of the cavity showing periodic particle orbits projected to the plane $y_W = 0$. The particle ($a = 0.05$, $\varrho = 1.0001$) can be trapped in different (from top to bottom) convective cells indicated by the cell index n. The cell boundaries can be identified from the faint streaklines made by fine aluminium flakes. Each exposure covers the time $t \in [65, 115]$ s. $T = 34.3\,°C$. The isolated white dots in the cell centres indicate the particle size. (*b*) Superposition of 36 individual particle trajectories (red), for a duration of 15 periods each, and mapped, using (2.2), to the generic convection cell $n = 0$ in comparison with the two closed streamlines (black). The arrows indicate the direction of the wall motion.
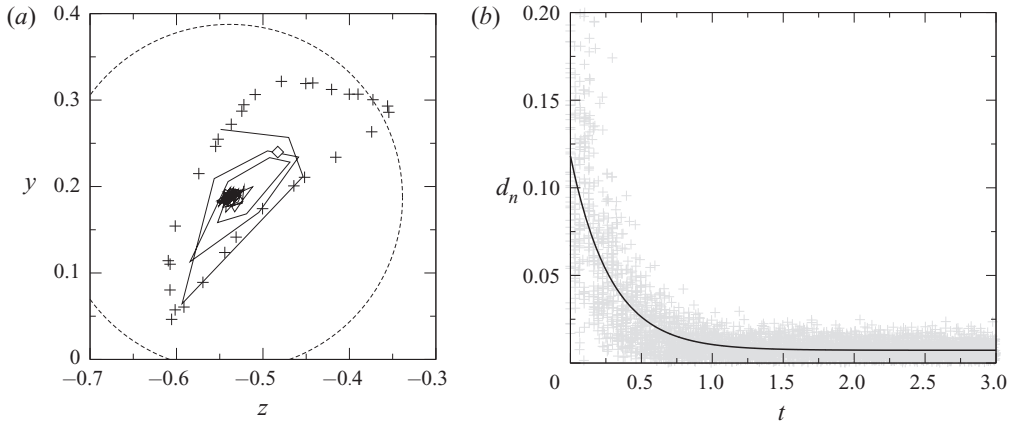
FIGURE 11. (*a*) Poincaré section on $x = 0$ with Poincaré points (y_n, z_n) connected by straight lines for $a = 0.05$ and $\varrho = 1.0001$. Also shown is the largest numerically reconstructible KAM torus (+) and the fixed point ($y^*, z^*)_{num} = (0.2340, -0.5254)$ corresponding to the closed streamline ($\Diamond$). The dashed line indicates the distance $d^* = 0.2$ from the experimental fixed point ($y^*, z^*)_{exp} = (0.1876, -0.5386)$. (*b*) Distance function $d_n = d(t_n)$ for 36 experimental realisations (+) and exponential fit $d(t)$ (full line), yielding the attraction rate $\bar{\sigma} = 3.5 \pm 0.1$ ($A = 0.111 \pm 0.002$, $B = 0.0073 \pm 0.0003$). The time is given in viscous units $H^2/\nu(T)$. $T = 34.3\,^\circ\text{C}$.

is the estimated fixed point corresponding to the limit cycle of the periodic attractor with N_{max} the total number of Poincaré points recorded. Considering the last $K = 20$ Poincaré points of the total sequence of points we define the time τ_I such that $d_n(t > \tau_I) < d^* = 0.2$. In the case of a quasi-periodic attractor (see further below) the same definition is used to estimate the geometric centre of the quasi-periodic attractor in the Poincaré plane.

With the 36 realisations of the experiment we find the average initial time scale to be $\bar{\tau}_I = 0.18$. This value is significantly less than the time $\tau_{relax} \approx 0.6$ the flow needs to fully relax to steady state (see above). This indicates the transfer of the particle from the chaotic sea to the regular region in case of a steady flow would be much faster than the viscous momentum diffusion across the length scale H of the flow.

Once the distance to the fixed point has dropped below $d_n < d^* = 0.2$ (dashed circle in figure 11*a*) the particle is always found to be attracted to the limit cycle without large excursions and the Poincaré points lie inside or very close to the main KAM torus. An example is shown in figure 11(*a*). Successive Poincaré points connected by lines show a spiralling-in convergence to the fixed point characterising the limit cycle. For comparison, the Poincaré section of the closed streamline and of a streamline on the largest reconstructible primary KAM torus are shown by a diamond ($\Diamond$) and pluses (+), respectively. The periodic particle orbit and its Poincaré section differ slightly from the ones of the closed streamline. In particular, the minimum distance of the attractor from the boundary (which occurs with respect to the moving wall near $x \approx -0.8$) is $\Delta_p^{x=-\Gamma/2} = 0.108$. This is larger than $\Delta_\psi^{x=-\Gamma/2} = 0.077$ (table 2) and also larger than $a = 0.05$, indicating a relatively large lubrication gap width $\delta \approx a$ between the surface of the particle and the moving wall.

The discrete distance function $d_n = d(t_n)$ is shown in figure 11(*b*) for 36 realisations of the experiment. Assuming the particle nearly follows the flow in the bulk, its trajectory between successive interactions with the moving walls will resemble the motion on KAM

tori with decreasing cross-sections in the case of a steady flow (Hofmann & Kuhlmann 2011). Due to the non-circular shape of the cross-section of the KAM tori and the two incommensurate frequencies characterising the motion on a KAM torus the discrete function d_n is not monotonic, but will decay in the mean. To find the mean asymptotic attraction rate to the limit cycle we fit the measured data (t_n, d_n) by

$$d(t) = A\mathrm{e}^{-\sigma t} + B, \tag{4.2}$$

where σ is the attraction rate and A and B are constants. The offset $B \neq 0$ is non-zero due to experimental uncertainties and the distance function $d_n \geq 0$ being positive. Also in the general case of attraction to a torus (see below) $B \neq 0$. To improve the statistics the fit shown in figure 11(b) is made using data from 36 realisations of the experiment. As can be seen the data are compatible with an exponential attraction to the limit cycle with an average attraction rate $\bar{\sigma} = 3.5 \pm 0.1$.

4.2. *Case $a = 0.011$*

A particle with $a = 0.011$, corresponding to $a_p = 0.45$ mm, and $\varrho = 1.0001$ can approach the moving walls closer than a particle with $a_p = 2.00$ mm studied above. Therefore, the length scale $\Delta = a + \delta$ over which the wall-induced forces act on the particle is smaller and the particle cannot be transferred to the same periodic attractor as for $a = 0.05$. The smaller particle is rather attracted to a quasi-periodic orbit which is similar to a particular KAM torus of the main KAM system, and which is tangent to a cylindrical surface at a distance Δ from the rotating cylinders (Hofmann & Kuhlmann 2011). Two representative particle trajectories (red) on the toroidal attractors are shown in figure 12(a) together with two streamlines on the largest reconstructible KAM tori (black). The tori to which the particles are attracted, and their corresponding counterparts in the other convection cells, are not the only types of attractors possible for nearly neutrally buoyant particles with $a = 0.011$. We also find period-five attractors shown in figure 12(b). They correspond to the secondary slender period-five sets of KAM tori of the unperturbed flow (blue in figure 6 above). The intricate structure of the period-five attractors is strikingly similar to the corresponding KAM tori.

Repeated experiments show that the particle is always attracted to one of the four attractors (two of each kind) in the generic convection cell. Figure 13(a) shows the superposition of all 32 individual trajectories measured. For clarity we use the naming convention P and QP for periodic and quasi-periodic attractors, respectively, numbers for the periodicity, and letters a and b to indicate the location of the attractor either near the cell boundary at $z = -\lambda/4 = -0.675$ or near $z = +\lambda/4 = 0.675$, respectively. The correspondence between the attractors found and the KAM tori is particularly clear from the Poincaré sections on $y = 0$ shown in figure 13(b) for the 32 individual trajectories on the period-one (red) and the period-five attractors (blue) in comparison to the largest reconstructible primary and period-five KAM tori (black dots). The location and shape of the experimental attractors agree well with the KAM tori.

In all 32 realisations of the experiment the particle initially moves in a chaotic fashion. Therefore, the toroidal particle attractors are typically approached from outside. Assuming 32 realisations of the experiment represent a sufficient sampling of the whole volume accessible to the particle, it is concluded that the four attractors found in the generic convection cell are the only ones for the given particle and flow parameters.

The amplitude spectra $\hat{X}$ and $\hat{Z}$ of representative particle trajectories $X = (X, Y, Z)$ shown in figure 14 confirm the particle either moves on a torus (figure 14a) or on a
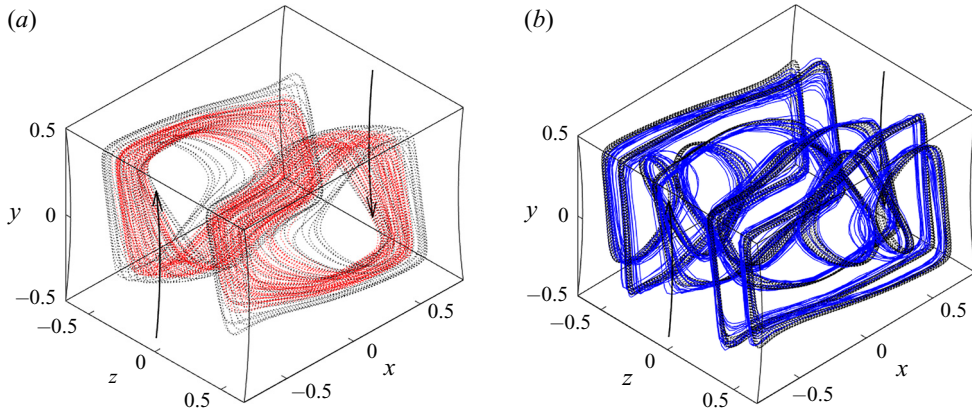
FIGURE 12. Particle trajectories for $a = 0.011$ ($a_p = 0.45$ mm) and $\varrho = 1.0001$ recorded during $t \in [300, 500]$ s. $T = 23.7\,^{\circ}$C. (*a*) Two point-symmetrically located quasi-periodic (toroidal) attractors (red), (*b*) two periodic attractors with period five (blue). Also shown are the corresponding largest reconstructible KAM tori (black) obtained numerically. The wall motion is shown by arrows.
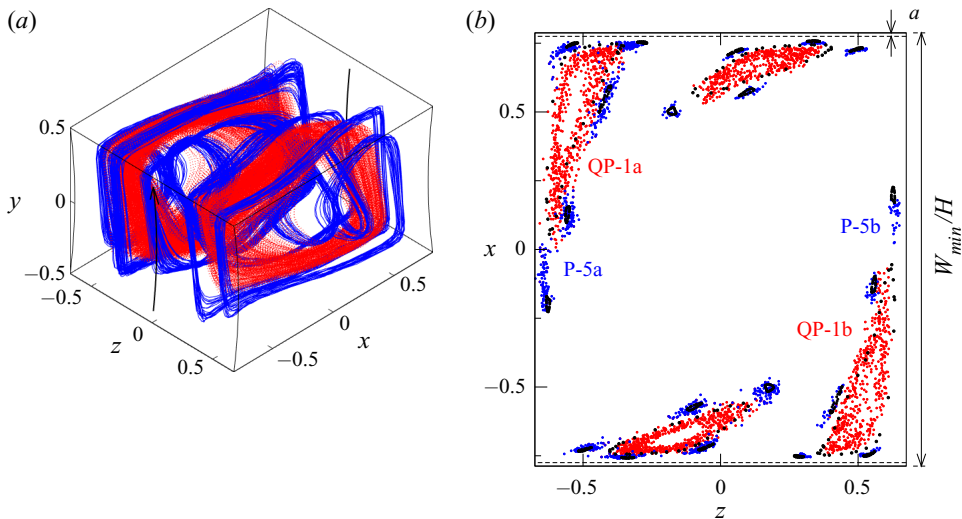

FIGURE 13. Thirty-two trajectories for $a = 0.011$ ($a_p = 0.45$ mm) and $\varrho = 1.0001$ recorded during $t \in [300, 500]$ s. $T = 23.7\,^{\circ}$C. (*a*) Three-dimensional view of the two toroidal period-one (red) and the two period-five attractors (blue) in the generic convection cell. (*b*) Poincaré sections on the plane $y = 0$ (red, blue) of the particle trajectories shown in (*a*). Poincaré sections of numerically computed streamlines on the corresponding largest reconstructible KAM tori are shown as black dots. The dashed lines indicate the distance a (particle radius) from the moving walls in the midplane $y = 0$.

periodic orbit (figure 14*b*). The spectrum for a particle on the toroidal attractor (red in figure 12*a*) exhibits two incommensurate frequencies. The largest peak at frequency $f_1 = 0.39$ Hz represents the vortex turnover motion in the cavity, corresponding to the toroidal direction. The minor peak at $f_2 = 0.0825$ Hz represents the winding frequency on the torus (poloidal direction). Other than these two frequencies only sums and differences
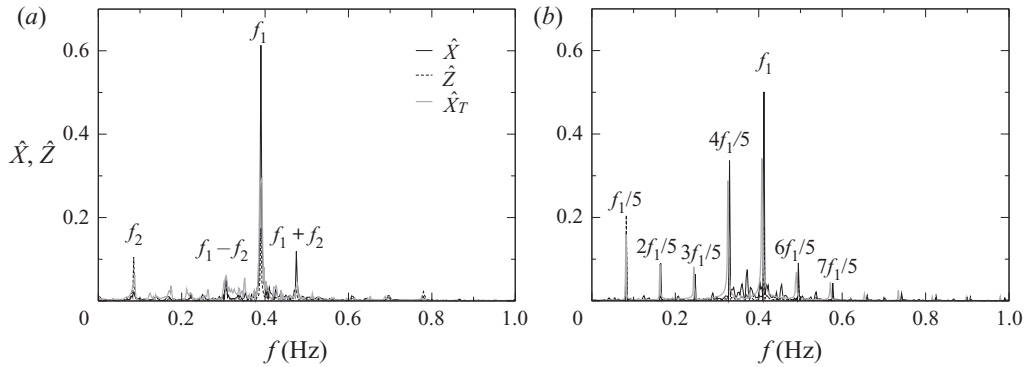
FIGURE 14. Amplitude spectra of the two particle-motion attractors for $a = 0.011$ ($a_p = 0.45$ mm) and $\varrho = 1.0001$. (a) Spectra $\hat{X}$ (full) and $\hat{Z}$ (dashed) for a trajectory on the tubular attractor with $f_1 = 0.39$ Hz ($F_1 = 31.39$) and $f_2 = 0.0825$ Hz ($F_2 = 6.64$), and spectrum $\hat{X}_T$ (grey) of a streamline on the largest numerically reconstructible KAM torus of period one. (b) Spectra $\hat{X}$ (full) and $\hat{Z}$ (dashed) of a trajectory on the period-five attractor with $f_1 = 0.4125$ Hz ($F_1 = 33.2$) and spectrum $\hat{X}_T$ (grey) of an intermediate reconstructible KAM torus of period five. $T = 23.7\,°C$.

of f_1 and f_2 contribute significantly to the spectrum. Therefore, the particle's motion is quasi-periodic. The amplitude spectrum of a trajectory on the period-five attractor (blue in figure 12b) is shown in figure 14(b). Again, the fundamental frequency $f_1 = 0.4125$ Hz is associated with the vortex turnover motion. In addition, the period-five character of the orbit is signalled by the presence of frequencies corresponding to the subharmonic of fifth order $f_1/5$ and its integer multiples. The experimental spectra of the particle trajectory agree very well with the spectrum of a streamline on the largest reconstructible KAM torus (grey in figure 14).

Figure 15 shows the Poincaré section on $x = 0$ for one representative trajectory on the toroidal attractor (lines). It nearly coincides with the largest numerically reconstructible KAM torus (+). Furthermore, the attraction rate $\bar{\sigma} = 1.2$ can be estimated from the exponential fit (4.2) to the data for d_n of 18 trajectories.

4.3. *Case $a = 0.025$*

For a particle with radius $a = 0.025$ ($a_p = 1.00$ mm), which is intermediate of the two previous particle sizes, the period-five attractor is absent. However, a quasi-periodic attractor exists, similar to the one for particle size $a = 0.011$. As before, the toroidal surface to which the trajectory of the nearly neutrally buoyant particle is attracted nearly coincides with one of the primary KAM tori (figure 16), albeit with a smaller cross-sectional area in the Poincaré plane than the one for the smaller particle with $a = 0.011$. The coincidence of the particle attracting torus with an intermediate KAM torus of the unperturbed flow is consistent with the particle–boundary interaction model (Hofmann & Kuhlmann 2011) in which a small neutrally buoyant particle is attracted to a KAM torus which is tangent to the surface which has a distance Δ from the moving walls. As the particle with radius $a = 0.025$ is larger, it is repelled at a larger distance Δ from the moving walls than the particle with $a = 0.011$. The same reason prevents the particle with $a = 0.025$ to be transferred to the slender period-five system of KAM tori which is apparently located too close to the moving wall for a particle with $a = 0.025$.
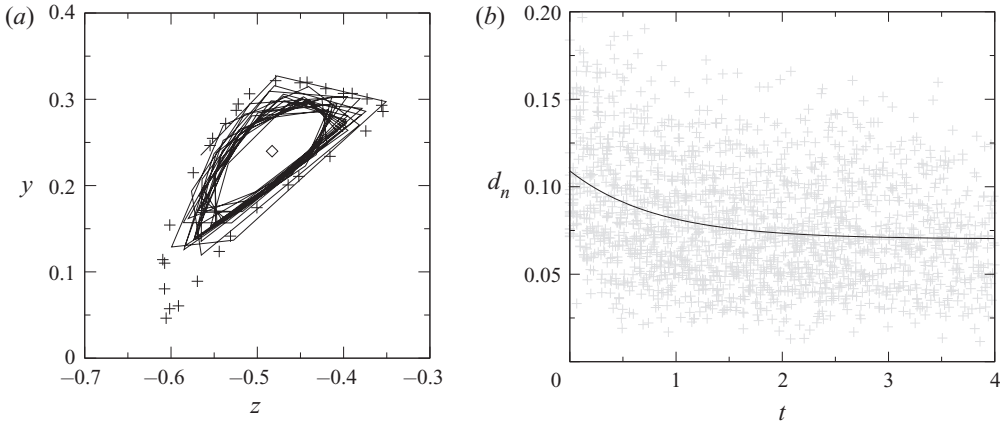
FIGURE 15. (*a*) Poincaré section on $x = 0$ with Poincaré points (y_n, z_n) connected by straight lines for $a = 0.011$ and $\varrho = 1.0001$. Also shown is the largest numerically reconstructible KAM torus (+) and the closed streamline ($\Diamond$). (*b*) Experimental distance function d_n for 18 experimental realisations (+). The exponential fit $d(t)$ (full line) yields the attraction rate $\bar{\sigma} = 1.2 \pm 0.4$ ($A = 0.04 \pm 0.006$, $B = 0.07 \pm 0.003$). The time is given in viscous units $H^2/\nu(T)$. $T = 23.7\,^{\circ}\text{C}$.
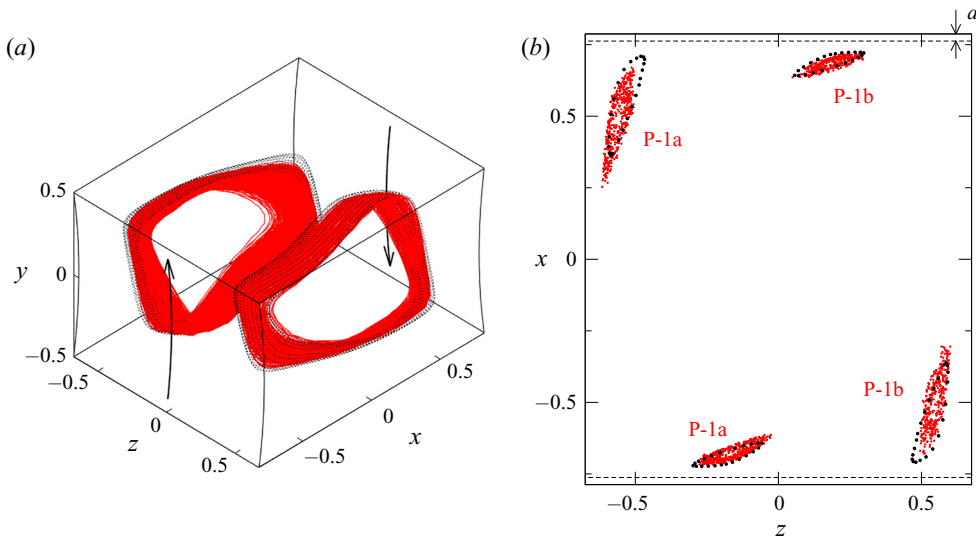

FIGURE 16. Superposition of 18 particle trajectories on the toroidal attractor for a particle with $a = 0.025$ ($a_p = 1.00$ mm) and $\varrho = 1.0001$. All trajectories were recorded during the period $t \in [300, 400]$ s. $T = 23.7\,^{\circ}\text{C}$. (*a*) Three-dimensional view of the trajectories (red) and numerically computed KAM torus of approximately the same size (dashed black lines). (*b*) Poincaré section on the plane $y = 0$ for the trajectories (red) shown in (*a*) and of streamlines (black dots) on an intermediate KAM torus (also shown before in figure 6*b*). The dashed lines indicate the distance a (particle radius) from the moving walls in the Poincaré plane.
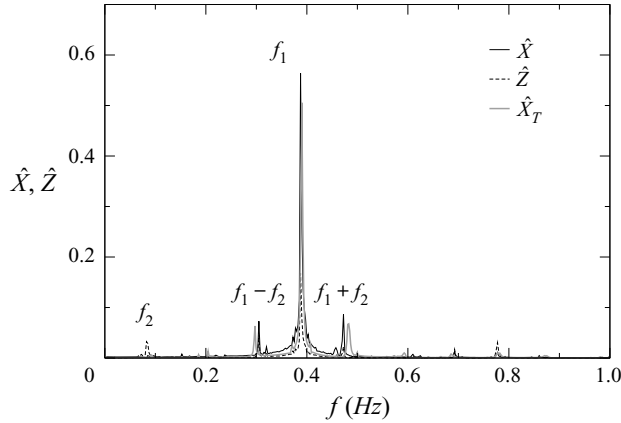
FIGURE 17. Amplitude spectra of the trajectory of a particle with $a = 0.025$ ($a_p = 1.00$ mm) and $\varrho = 1.0001$ moving on its toroidal attractor. Shown are the spectra $\hat{X}(f)$ (solid line) and $\hat{Z}(f)$ (dashed line). The dominant frequencies are $f_1 = 0.3875$ Hz ($F_1 = 30.96$) and $f_2 = 0.0825$ Hz ($F_2 = 6.59$). The spectrum $\hat{X}_T$ of a streamline on a corresponding intermediate KAM torus of period one is shown in grey. $T = 23.7\,^{\circ}$C.

The quasi-periodic motion of the particle on the toroidal attractor is confirmed by the amplitude spectra of the x and z coordinates of its trajectory $X(t)$. We find two incommensurate frequencies with the main toroidal frequency $f_1 = 0.3875$ Hz, the poloidal frequency $f_2 = 0.0825$ Hz, and their sum and difference (figure 17).

The transient motion near the quasi-periodic toroidal attractor in the Poincaré plane $x = 0$ is shown in figure 18 (lines) in comparison with the largest reconstructible primary KAM torus (pluses). Analysing 18 realisations of the experiment (not shown) the attraction rate is $\bar{\sigma} = 2.3 \pm 0.3$. The mean transient time to reach the attractor up to the distance $d_n \leq 0.2$, determined by (4.1), is $\bar{\tau}_I = 0.9$, comparable to the viscous diffusion time scale τ_v.

4.4. *Case $a = 0.039$*

Further increasing the particle size to $a = 0.039$ ($a_p = 1.58$ mm) the particle finds its attractor in form of a very slender torus corresponding to a very slender KAM tube. The particle trajectories for 52 experimental realisations (red) and a slender numerical KAM torus (black) which closely encircles the closed streamline are shown in figure 19. Due to the small diameter of the attracting toroidal surface experimental imperfections prevent distinguishing it from a periodic orbit in the Poincaré section (figure 19b). However, from the spectrum of the particle's trajectory (figure 20) the quasi-periodic particle motion can be clearly perceived. Two primary peaks at the two incommensurate frequencies $f_1 = 0.375$ Hz and $f_2 = 0.0825$ Hz arise in the spectrum for a single-particle trajectory. Also the sum and difference frequencies are present with small amplitude. While the turnover motion with frequency f_1 dominates the trajectory, the amplitude of the poloidal motion at f_2 is very small. Analysing the transient behaviour for 52 single-particle experiments (figure 21b) the average attraction rate is found to be $\bar{\sigma} = 2.9 \pm 0.1$. A representative transient trajectory is shown in figure 21(a) in the Poincaré plane $x = 0$.

The attracting torus for $a = 0.039$ is very slender and the situation is close to the tangent case of Hofmann & Kuhlmann (2011). Observing that the smaller particle with $a = 0.011$
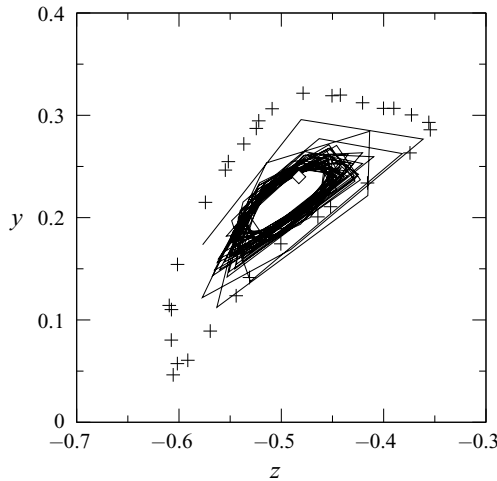
FIGURE 18. Final phase of the spiralling-in attraction of a particle ($a = 0.025$, $\varrho = 1.0001$) to its toroidal attractor. Shown are successive Poincaré points connected by lines, recorded during $t \in [117, 496]$ s. $T = 23.7\,^\circ$C. Pluses ($+$) and diamond ($\diamond$) indicate the largest numerically reconstructible KAM torus and closed streamline, respectively.

is attracted to a torus close to the largest reconstructible KAM torus (figure 15a) one can estimate the tangent case will arise for a particle with $a \approx 0.041$. In this case the attractor would be periodic, approximating the closed streamline. The larger particle with $a = 0.05$ (§ 4.1) is also attracted to a periodic orbit. But this orbit (figure 11a) is more distant from the closed streamline than the nearly periodic orbit for $a = 0.039$ (figure 21a). This is consistent with the model of Hofmann & Kuhlmann (2011) according to which particles larger than the optimum ones (corresponding to the tangent case) are also attracted to periodic orbits. These periodic orbits, however, lie on a KAM torus and they are closed during the particle–boundary interaction process.

4.5. *Case $a = 0.004$ and $\varrho = 1.003$*

Finally, we consider the smallest particle, with radius $a = 0.004$ ($a_p = 0.15$ mm) and with a density mismatch of 0.3 % ($\varrho = 1.003$). This particle, as well as all particles with $\varrho = 1.0001$ considered before, are essentially advected in the bulk, because the leading-order inertial effect scales with the small factor $(\varrho - 1)St_{conv}$ (see also (5.1) below), where $St_{conv} = StRe$ is the convectively scaled Stokes number. For $a = 0.004$ and $\varrho = 1.003$ one obtains $(\varrho - 1)St_{conv} = 4.3 \times 10^{-6}$, and for the largest particle investigate with $a = 0.071$ and $\varrho = 1.0001$ the inertial force scales like $(\varrho - 1)St_{conv} = 4.5 \times 10^{-5}$. Note, however, that all particles initially being advected along chaotic streamlines will eventually interact with the moving walls, regardless of their size.

The small particle with $a = 0.004$ and $\varrho = 1.003$ is found to be essentially advected by the flow. We find the particle always moves in the region occupied by chaotic streamlines and it is never attracted to a periodic or quasi-periodic orbit. Since the distance of the KAM tori from the moving walls is ~ 7 times larger than the particle radius (see table 2), the length scale $\Delta = a + \delta = O(10^{-3})$, over which the wall effect on the particle is significant, is too small to transfer the particle to the region of the flow occupied by KAM tori. Therefore, a focusing of the particle's trajectory is not possible via the boundary interaction process. Yet, the particle will experience the wall effect which will
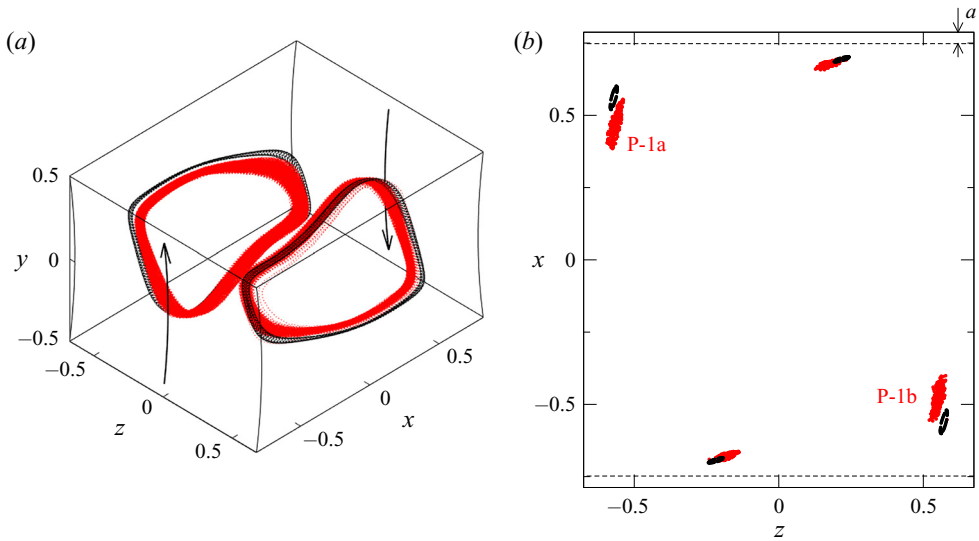
H. Wu, F. Romanò and H. C. Kuhlmann

FIGURE 19. Superposition of 52 particle trajectories for a particle with $a = 0.039$ ($a_p = 1.58$ mm) and $\varrho = 1.0001$. All trajectories were recorded during $t \in [300, 400]$ s. $T = 26.1\,°C$. (*a*) Three-dimensional view of the particle trajectories (red) and two very slender KAM tori calculated numerically (black dotted lines). (*b*) Poincaré section on $y = 0$ of 52 particle trajectories (red) and of streamlines (black) on two slender KAM tori. The dashed lines indicate the distance a from the moving walls in the Poincaré plane $y = 0$.
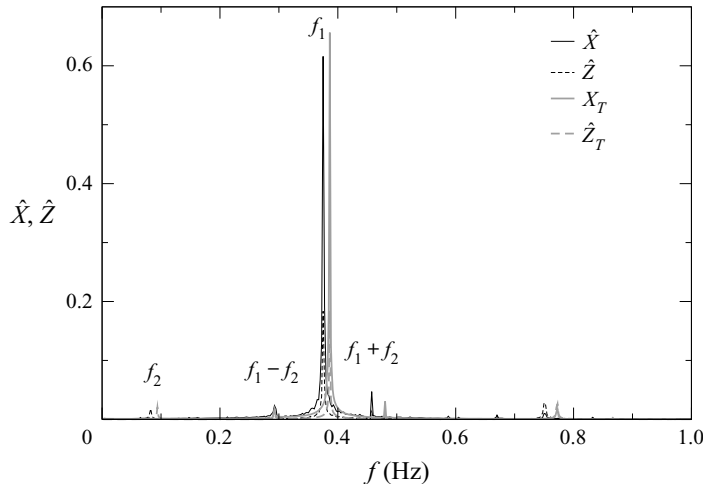

FIGURE 20. Amplitude spectra of the trajectory $X(t)$ of a particle with $a = 0.039$ and $\varrho = 1.0001$. Shown are $\hat{X}$ (full line) and $\hat{Z}$ (dashed line). The main frequencies are $f_1 = 0.375$ Hz ($F_1 = 30.96$) and $f_2 = 0.0825$ Hz ($F_2 = 6.81$). Also shown are spectra $\hat{X}_T$ and $\hat{Z}_T$ of a streamline on a very slender KAM torus with period one (shown in figure 19), located near the closed streamline. $T = 26.1\,°C$.
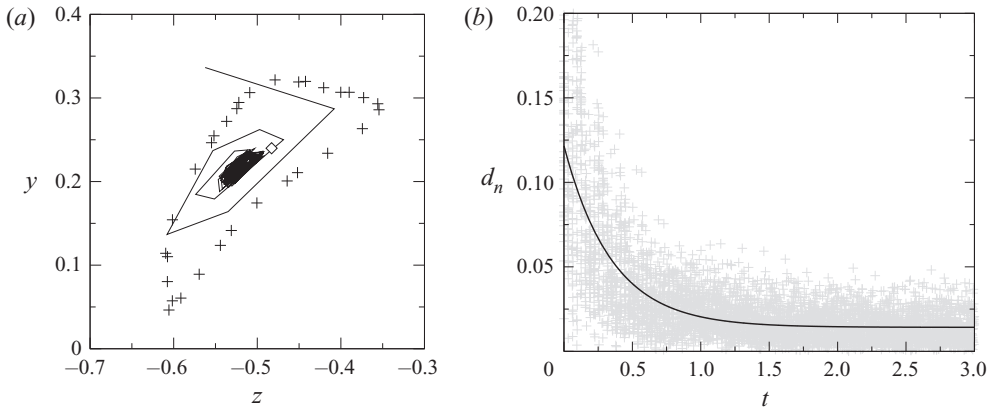
FIGURE 21. (*a*) Attraction to a quasi-periodic orbit of a particle with $a = 0.039$ ($a_p = 1.58$ mm) and $\varrho = 1.0001$ (lines) in comparison to the largest reconstructible KAM torus of the flow (+) and the closed streamline ($\Diamond$). (*b*) Distance function d_n for 52 realisations as functions of time and fit $d(t)$ of the distance functions according to (4.2), yielding the attraction rate $\bar{\sigma} = 2.9 \pm 0.1$.

merely displace the particle from some incoming chaotic streamline to another outgoing chaotic streamline and the particle will continue to explore the region occupied by chaotic streamlines (see, however, Kuhlmann & Muldoon (2013) and Muldoon & Kuhlmann (2013), for particle attractors in the chaotic region of the flow).

The motion of individual particles with $a = 0.004$ has been recorded for $t \in [0, 8250]$ s. Two trajectories are shown in figure 22(*a*), distinguished by colour. The two particles stay in a single convection cell and each of them seems to explore one half of the whole volume occupied by chaotic streamlines which extends up to all boundaries of the cell. Under the idealising assumption that the particle is perfectly advected in the bulk, it may not, however, populate those chaotic streamlines which originate from the layer on the (moving) walls which is inaccessible for the particle centroid. This depletion effect, which has been found in other systems as well (Muldoon & Kuhlmann 2013; Kuhlmann *et al.* 2014; Orlishausen *et al.* 2017; Romanò & Kuhlmann 2019), is visible in figure 22(*a*) on the walls at $y = \pm 0.5$ just upstream of the moving walls and results from the deceleration, thus widening, of the layer of streamlines from the inaccessible layers on the moving walls. Regardless of the depletion effect in the region of chaotic streamlines, the particles do not enter the regions occupied by KAM tori. This is clearly seen from the Poincaré section on $y = 0$ shown in figure 22(*b*) in which patches devoid of Poincaré points arise. The four empty patches corresponding to the two primary KAM tori are evident. For comparison the Poincaré sections for the two largest reconstructible KAM tori of period one have been included as squares.

The Poincaré section in figure 22(*b*) compares qualitatively with the numerical Poincaré section of streamlines computed by Romanò & Kuhlmann (2017*b*) in their figure 12 for a rectangular cavity with $\Gamma = 1.7$ and $Re = 500$. The central region of the Poincaré plane is not populated by Poincaré points. This effect may be due to the flow topology: The centre of the cell at $(x, y, z) = (0, 0, 0)$ hosts a spiralling-in saddle focus c whose stable manifold originates from a degenerate wall limit cycle w_c (figure 9 of Romanò *et al.* 2017). Since the streamlines originating from the near-wall region are depleted of particles, these cannot move in the vicinity of the stable manifold of c. This interpretation is confirmed by noticing that the stable two-dimensional manifold of the spiralling-in saddle focus c
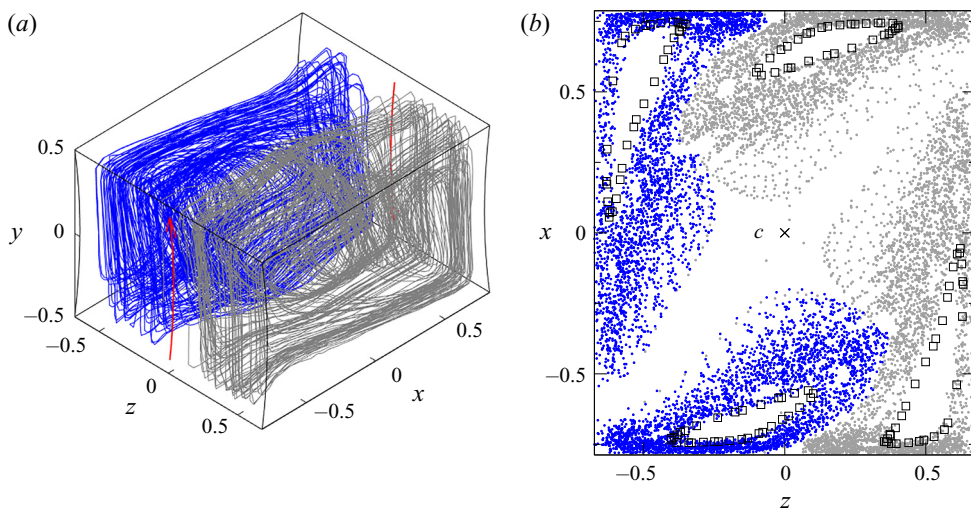
H. Wu, F. Romanò and H. C. Kuhlmann

FIGURE 22. (*a*) Trajectories of two particles with $a = 0.004$ ($a_p = 0.15$ mm) and $\varrho = 1.003$ distinguished by colour (grey and blue) and shown for $t \in [0, 500]$ s. (*b*) Poincaré section on the plane $y = 0$ for both particles during $t \in [0, 8250]$ s and largest reconstructible period-one KAM tori (squares). The cross ($\times$) denotes the spiralling-in saddle focus c in the flow. $T = 26.7\,^{\circ}$C.

represents a transport barrier for perfect tracers inside the convection cell. The barrier is almost respected by the present particles: the particle (blue) moving in the left part of the cell in figure 22(*b*) did not visit the right region throughout the whole observation time. Similarly, the particle (grey) moving in the right region in figure 22(*b*) stays there for a long time. Careful inspection of figure 22(*b*), however, shows that the particle in grey colour has crossed the transport barrier of the steady flow once during the late stage of the trajectory shown. The rare crossing of the flow barrier by the particle may be due to experimental imperfections or due to the particle not being a perfect tracer.

The chaotic motion of the particles can also clearly be identified by the amplitude spectra of a typical trajectory shown in figure 23. As expected, the spectra are broadband, but four peaks characteristic for a torus-like motion are still visible. The long period of time of 8250 s during which the small particle continues to move chaotically compared to the much shorter period of time of the order of $O(300$ s) during which the larger particles become attracted to periodic or quasi-periodic orbits, is yet another proof that the strong attractors for the motion of larger particles are caused by the particle–boundary interaction.

4.6. *Synthesis of results for nearly neutrally buoyant particles*

The attractors found for the motion of nearly neutrally buoyant particles of different sizes and moderate Stokes numbers are all created by particle–boundary interaction due to the finite particle size. The rates of attraction during the second, asymptotic phase of the particle motion are summarised in figure 24 as function of the particle radius $a = [0.011, 0.025, 0.039, 0.050, 0.059, 0.071]$ (respectively $a_p = [0.45, 1.00, 1.58, 2.00, 2.37, 2.85]$ mm). The data for $\bar{\sigma}(a)$ should not be interpolated, because the existence of finite-particle-size attractors is only possible if there exists a system of KAM tori which can receive the particles, i.e. whose distance from the boundary is compatible with the particle–boundary interaction length which, in turn, depends on the particle radius a. Nevertheless, the attraction rate is larger the larger the particle is.
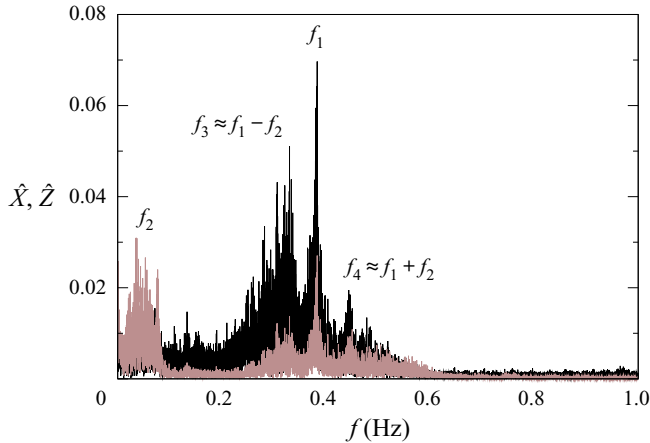
FIGURE 23. Amplitude spectra $\hat{X}$ (black) and $\hat{Z}$ (brown) of the trajectory of a single particle with $a = 0.004$ ($a_p = 0.15$ mm) and $\varrho = 1.003$ (the grey particle in figure 22). The frequency peaks of $\hat{X}$ are $f_1 = 0.3833$ Hz, $f_2 = 0.05318$ Hz, $f_3 = 0.3301$ Hz $\approx f_1 - f_2$ and $f_4 = 0.4439$ Hz $\approx f_1 + f_2$. $T = 26.7\,^{\circ}$C.
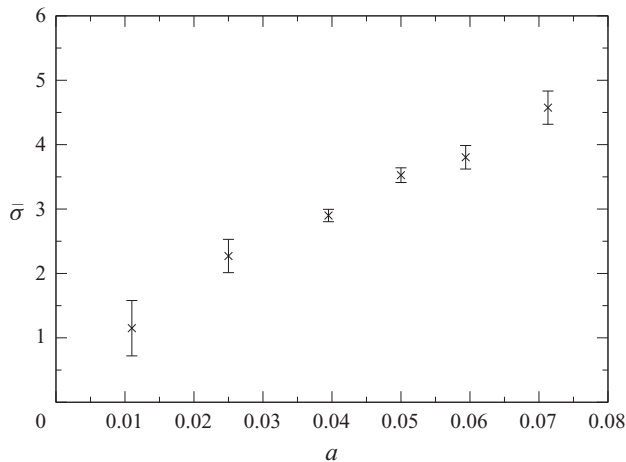

FIGURE 24. Mean attraction rates $\bar{\sigma}$ to the attractors for nearly neutrally buoyant particles ($\varrho = 1.0001$) with radii $a = 0.011, 0.025, 0.039, 0.050, 0.059$ and 0.071, corresponding to $a_p = 0.45$ mm, 1.00 mm, 1.58 mm, 2.00 mm, 2.37 mm and 2.80 mm.

An estimate, provided in appendix B, of the attraction rate of neutrally buoyant particles to periodic orbits based on the inelastic collision model of Hofmann & Kuhlmann (2011) applied to the present flow and particle parameters $a = 0.05$ and $\varrho = 1.0001$ yields $\sigma = 20$, larger than the measured value. Likewise, the rates of attraction for neutrally buoyant particles found numerically in a similar flow (a rectangular two-sided cavity with straight moving walls, Romanò *et al.* 2019*a*) are much larger ($\sigma \approx 30$) than our experimental measurements. The too small experimental attraction rates, as compared to the theoretical and numerical results, are most likely related to the fact that in the model of Hofmann & Kuhlmann (2011) and in the numerics of Romanò *et al.* (2019*a*) the particle is introduced velocity matched to the fully developed steady flow. Therefore, the attraction

dynamics is independent of the relaxation time scale of the flow. In our experiments, however, the particle motion is analysed from $t = 0$ and, therefore, is strongly affected by the initial flow transient during which the initially unordered flow decays to the steady flow on a viscous time scale. From figure 7(*b*) we find the dimensionless relaxation rate of the flow as $\sigma_{flow} = 6.9$. It is not surprising that the attraction rates are all (slightly) less than σ_{flow}, because the dynamics of nearly density-matched particles is slaved to that of the flow. It is thus concluded that the flow transient reduces the particle attraction rates obtained in an ab-initio fully developed steady flow to those measured for the present transient flow.

Figure 25 combines the particle motion attractors for nearly neutrally buoyant particles within a single Poincaré section for the generic convection cell. The particle radius, indicated by colour, ranges from $a = 0.004$ to 0.071 ($a_p = 0.15$ mm to 2.80 mm). All attractors are located in the region occupied by regular streamlines. For very small particle radii the particle moves chaotically. As the particle radius increases quasi-periodic attractors are created. On a further increase of a, the distance of the quasi-periodic attractors from the moving walls increases. Based on the shrinking cross-sections of the quasi-periodic attractors with particle size the first appearance of a periodic attractor is expected for $a = a_{tangent} \approx 0.041$. The location of this orbit should lie in the centre of the yellow point clouds ($a = 0.039$) in figure 25. This situation corresponds to the so-called tangent case of Hofmann & Kuhlmann (2011) (their section V.A.1) in which the attractor becomes periodic and approaches the closed streamline inside of the KAM tori. The reverse scenario, upon decreasing a, resembles the Ruelle–Takens–Newhouse scenario for the transition to turbulence (Newhouse, Ruelle & Takens 1978). However, we could not unambiguously determine a third incommensurate frequency in the spectrum of the particle with $a = 0.004$ (figure 23), hence we conclude that our experiment does not fall in the class of the Ruelle–Takens–Newhouse scenario. The absence of a third incommensurate frequency is consistent with the model of Hofmann & Kuhlmann (2011) which predicts an abrupt change of the particle motion from a quasi-periodic to a chaotic motion, in which the particle is fully slaved to the flow field and no physical reason exists for a third incommensurate frequency.

For particles larger than $a = a_{tangent}$ (in the sense of Hofmann & Kuhlmann 2011), periodic attractors are expected as well. This is confirmed by our experiments. The deviation of the periodic orbit for the large particle with $a = 0.05$ ($a_p = 2.00$ mm) (figure 25) from the closed streamline in the tangent case is expected. According to the model of Hofmann & Kuhlmann (2011) the periodic orbits for these larger particles lie on KAM tori in the bulk and are only closed by small trajectory segments near the boundary where the particle experiences the boundary effect. For particles larger than $a = 0.05$ temperature-controlled density matching becomes increasingly delicate. But we do find periodic attractors also for particles with $a = 0.59$ ($a_p = 2.37$ mm) and $a = 0.71$ ($a_p = 2.85$ mm), both with density ratio $\varrho = 1.0001$. The Poincaré sections of their periodic orbits are included in figure 25. The spectra of these orbits (not shown) confirm the orbits are periodic. This is different from attractors in thermocapillary liquid bridges for which period-doubled attractors have been predicted by Mukin & Kuhlmann (2013) for sufficiently large particles, and observed experimentally by Gotoda *et al.* (2019).

By tracking particles with different sizes, we could effectively visualise the flow topology experimentally. In particular, those KAM tori which are located in the vicinity of the moving walls can be targeted. In the present steady flow all KAM tori approach the moving walls sufficiently close such that they can attract suitably sized particles to their vicinity. This interpretation is confirmed by comparing the particle motion attractors from figure 25 with the streamline topology obtained numerically and displayed in figure 6(*b*). Several properties of the attracting orbits for nearly density-matched particles are collected
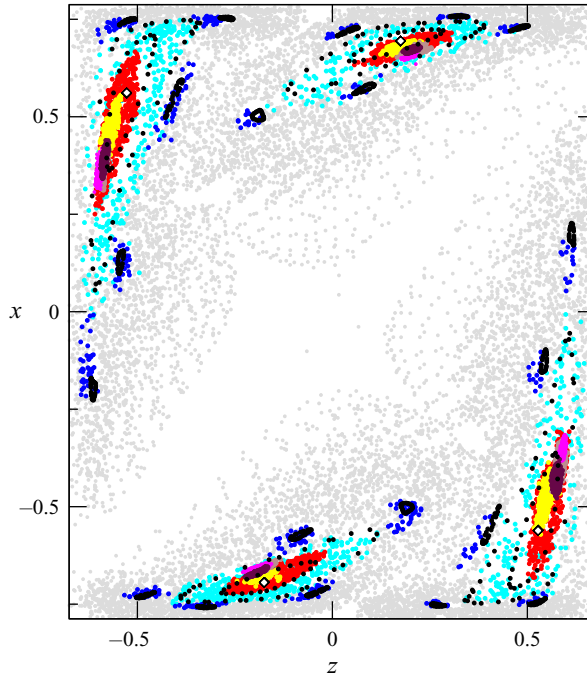
FIGURE 25. Overlay of Poincaré sections of trajectories of nearly neutrally buoyant spherical particles moving on their respective attractors. The colour indicates the particle radius: $a_p = 0.45$ mm (cyan and blue), 1.00 mm (red), 1.58 mm (yellow), 2.00 mm (brown), 2.37 mm (maroon) and 2.85 mm (magenta). Particles with $a_p = 0.15$ mm (grey) move chaotically in the chaotic sea. For comparison, the Poincaré section of KAM tori and of closed streamlines are shown as black dots and diamonds, respectively.

in table 3. Note the orbit time of the period-five attractor is $5\bar{\tau}_1$. The minimum distance of the attracting orbit with any boundary is always made with respect to a moving boundary. The mean winding angle $\bar{\theta}$ is experimentally determined by averaging the angles which two consecutive Poincaré points make in the plane $y = 0$ with the fix point or the geometric centre of the quasi-periodic attractor according to (4.1b).

From table 3 the initial transient time $\bar{\tau}_I$ required to approach the attractor up to the distance $d_n \leq 0.2$ (in the plane $y = 0$) increases when the particle size decreases. This effect can be explained by the thickness of the layer on the moving walls over which a small particle experiences forces from the boundary becoming thinner the smaller the particle. As the layer thickness shrinks also the overlap of the KAM tori with this layer shrinks, and the probability for a particle to be transferred to the KAM torus becomes lower. Therefore, small particles spend more time in the chaotic sea before being caught by a KAM torus.

Even though $a = 0.011$ appears to be a particle size compatible with a period-nine attractor, no attractors other than P-5 and QP-1 are observed. This might be related to the KAM torus of period five approaching the moving walls the closest (table 2), while a possible period-nine attractor has to compete with the period-one attractor which is based on the largest system of KAM tori. But the detailed dynamics, even within the collision model, can be quite complicated (Mukin & Kuhlmann 2013).

a	0.011	0.011	0.025	0.039	0.050	0.059	0.071
Type	P-5	QP-1	QP-1	QP-1	P-1	P-1	P-1
St	2.69×10^{-5}	2.69×10^{-5}	1.39×10^{-4}	3.38×10^{-4}	5.56×10^{-4}	7.74×10^{-4}	1.12×10^{-3}
St_{conv}	1.08×10^{-2}	1.08×10^{-2}	5.56×10^{-2}	1.35×10^{-1}	2.22×10^{-1}	3.09×10^{-1}	4.48×10^{-1}
f_1 [Hz]	0.4125	0.3900	0.3875	0.3750	0.3100	0.3475	0.3400
F_1	33.20	31.39	30.96	30.96	30.49	29.33	29.09
τ_1	0.0301	0.0319	0.0323	0.0323	0.0328	0.0341	0.0343
$\bar{\tau}_I$	—	2.8	0.9	0.3	0.2	0.2	0.2
$\bar{\sigma}$	—	1.2	2.3	2.9	3.5	3.8	4.6
$\bar{\theta}$	—	1.40	1.36	1.31	1.22	1.14	1.10
$\Delta_p^{y=0.5}$	0.061	0.073	0.102	0.129	0.143	0.132	0.129
$\Delta_p^{y=-0.5}$	0.044	0.061	0.096	0.108	0.135	0.159	0.159
$\Delta_p^{x=-\Gamma/2}$	0.039	0.058	0.078	0.096	0.107	0.118	0.127
$\Delta_p^{x=\Gamma/2}$	0.042	0.065	0.919	0.115	0.143	0.162	0.185
N	—	18	18	52	36	23	16

TABLE 3. Properties of measured trajectories on the attractor for nearly neutrally buoyant particles with $\varrho = 1.0001$ as function of the particle radius a. Specified are the type of attractor (P: periodic, QP: quasi-periodic), the Stokes number St, the convectively scaled Stokes number $St_{conv} = Re\,St$, fundamental frequencies f_1(dimensional) and F_1(dimensionless), turnover time $\tau_1 = F_1^{-1}$, initial transient time $\bar{\tau}_I$ required to approach the attractor up to the distance $d_n \leq 0.2$ (in the plane $y = 0$), asymptotic attraction rate $\bar{\sigma}$, mean winding angle $\bar{\theta}$ (modulo 2π), the closest wall-normal distances from the boundaries Δ_p (the boundary is indicated by the superscript) and the number of samples N used for averages.

5. Inertial particles

When the normalised density deviation $|\varrho - 1|$ between the particle and the liquid increases from zero, inertial and buoyancy forces may have to be taken into account. Expanding the Maxey–Riley equation (Maxey & Riley 1983) for small particles up to order $O(a^2)$ Lasheras & Tio (1994) obtained the inertial equation for the centroid $X(t)$ of a small particle

$$\dot{X} = u - (\varrho - 1)St\left(\frac{\mathrm{D}u}{\mathrm{D}t} + \frac{e_y}{Fr^2}\right), \tag{5.1}$$

where $\mathrm{D}/\mathrm{D}t$ is the material derivative following the motion of the fluid and the acceleration of gravity acts in the negative y direction (e_y: unit vector in positive y direction). For convenience the diffusively scaled Froude number $Fr = \sqrt{\nu^2/(gH^3)} = 7.95 \times 10^{-4}$ at $T = 25\,°\mathrm{C}$ has been introduced, independent of ϱ and a_p, where g is the acceleration due to gravity. The Froude number based on the wall velocity ΩR and the sedimentation velocity is $Fr' = 9\nu^2 Re/[2(\varrho - 1)ga_p^2 H]$. The minimum and maximum values encountered are $min(Fr') = 99.4$ ($a_p = 0.48$ mm, $\varrho = 1.08$) and $max(Fr') = 9.05 \times 10^4$ ($a_p = 0.45$ mm, $\varrho = 1.0001$), respectively.

From the inertial equation (5.1) the leading-order effect of inertia and buoyancy on the velocity of the particle relative to the velocity of the fluid can be measured by $(\varrho - 1)St$ and $(\varrho - 1)St/Fr^2$, respectively. Both terms scale with a^2 and can become significant for the present millimetric particles, even if the density mismatch $|\varrho - 1|$ amounts to only a few per cent.
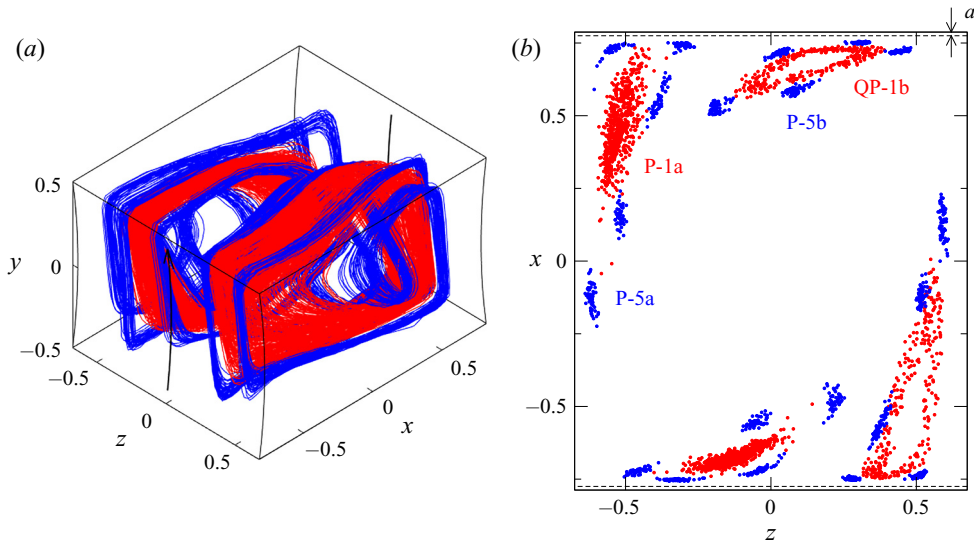
FIGURE 26. Thirty-nine trajectories of a particle with $a = 0.012$ ($a_p = 0.50$ mm) and $\varrho = 1.023$ recorded during $t \in [300, 400]$ s. $T = 26\,°C$. (*a*) Three-dimensional representation. (*b*) Poincaré section on the plane $y = 0$. The different attractors are distinguished by colour and labels.

5.1. *Case $a = 0.012$, $\varrho = 1.023$*

For the moderate density ratio $\varrho = 1.023$ the trajectories of single particles with $a = 0.012$ ($a_p = 0.50$ mm) and Stokes number $St = 3.8 \times 10^{-5}$ are still found to be attracted to particular orbits. Thirty-nine trajectories, each obtained from a single-particle experiment and recorded during $t \in [300, 400]$ s, are shown in figure 26(*a*). They are similar to those for $a = 0.011$ ($a_p = 0.45$ mm) and $\varrho = 1.0001$: the particle can be attracted either to one of two period-five structures (blue) similar to the corresponding sets of slender KAM tori, or to one of two structures (red) resembling the main period-one KAM tori.

More details can be recognised from the Poincaré section on $y = 0$ shown in figure 26(*b*). The trajectories of the particles attracted to the period-five structure (blue) seem to be independent of whether they are attracted near the one or the other point-symmetrically located KAM torus of period five existing in the generic convection cell. However, the two attractors forming near the two main KAM tori are different. One of the two attractors (QP-1b, on the right side of figure 26*b*) is clearly quasi-periodic, while the other one (P-1a, on the left side of figure 26*b*) seems to evolve into a periodic attractor. The distinction between the periodic and the quasi-periodic attractors becomes clearer when tracking particles for a much longer time. To that end two particles were tracked up to $t = 4980$ s, one being initiated in the left and the other one in the right half of the convection cell. During their evolution, the particles were found to always stay in the same half of the convection cell and, after one hour, the periodic and the quasi-periodic attractors are clearly established. Figure 27(*a*) shows the two trajectories for large times, i.e. during $t \in [4500, 4980]$ s. The Poincaré section on $y = 0$ in figure 27(*b*) displays all Poincaré points during $t \in [0, 4980]$ s (83 min since $t = 0$).

The evolution of the trajectories can thus be described by three phases: in the very short initial phase the particles are very rapidly transported to the region of the KAM tori. In the second phase they tend to focus on quasi-periodic orbits resembling a KAM torus on
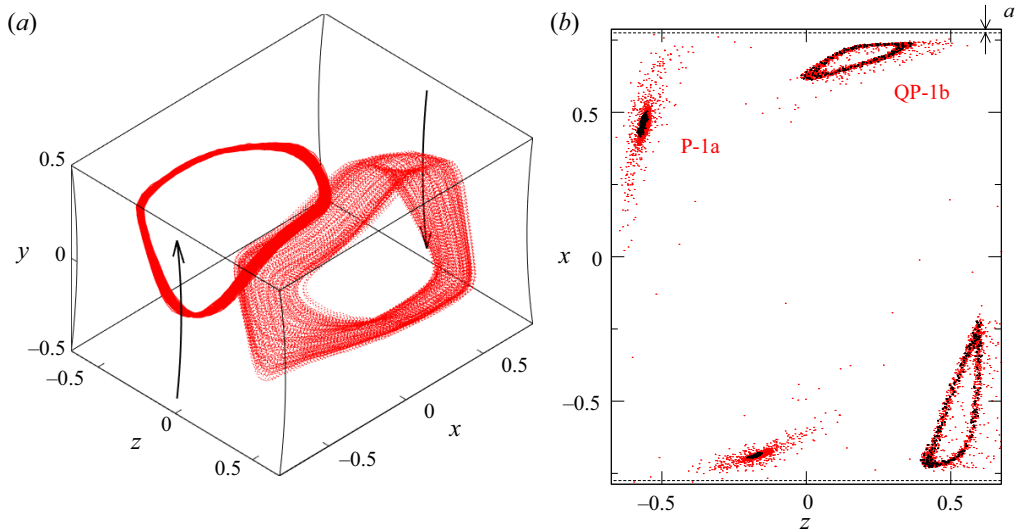
FIGURE 27. Trajectories of two particles with $a = 0.012$ ($a_p = 0.50$ mm) and $\varrho = 1.023$ approaching P-1a and QP-1b. (*a*) Three-dimensional view, $t \in [4500, 4980]$ s. (*b*) Poincaré points for the same particles during the full time interval $t \in [0, 4980]$ s (red) and during the final phase $t \in [4500, 4980]$ s (black). $T = 26\,^\circ$C.

a time scale comparable to that for density-matched particles. During the third phase, on a much longer time scale, the symmetry between the particles moving near the one or the other point-symmetrically located KAM torus is broken. One trajectory evolves to a limit cycle in the vicinity of the closed streamline of one KAM torus, while the other trajectory is stabilised on a quasi-periodic orbit near the other KAM torus.

To understand this behaviour, we consider symmetries and time scales. Inertial effects can lead to clustering on limit cycles or tori in steady solenoidal flows (see, e.g. Sapsis & Haller 2010). In particular, the dissipative character of inertial forces changes the structurally unstable trajectories along the closed streamlines into limit cycles which are either attracting or repelling (Kuhlmann & Muldoon 2012). The asymmetry of the evolution of the two particle trajectories in the present system, however, cannot be explained by inertial forces alone, because the flow field $\boldsymbol{u}$ and the inertia term $\mathrm{D}\boldsymbol{u}/\mathrm{D}t$ in (5.1) are both point symmetric with respect to the cell centre (see also Blohm & Kuhlmann 2002). The point symmetry

$$(x, y, z, u, v, w) \longrightarrow -(x, y, z, u, v, w), \tag{5.2}$$

corresponds to a rotation by π about the z-axis and a reflection with respect to the plane $z = 0$. Thus in the absence of buoyancy, i.e. under zero-gravity conditions, the particle evolution according to (5.1) should be the same near both point-symmetrically located closed streamlines such that the two invariant structures must either both be attracting or both be repelling. Therefore, the buoyancy term which does not satisfy the symmetry (5.2) is responsible for the symmetry breaking. Since the buoyancy term in (5.1) is solenoidal, it cannot, however, contribute to the contraction rate which amounts to $\nabla \cdot \boldsymbol{X} = -(\varrho - 1)St\nabla \cdot (\boldsymbol{u} \cdot \nabla \boldsymbol{u})$ independent of Fr.

Buoyancy forces on the particle are always associated with inertia forces. Inertia converts the closed trajectories along closed streamlines into limit cycles and buoyancy breaks the symmetry of these limit cycles such that one limit cycle is attracting and the

Attractor	$\Delta_p^{y=0.5}$	$\Delta_p^{y=-0.5}$	$\Delta_p^{x=-\Gamma/2}$	$\Delta_p^{x=\Gamma/2}$
P-1a	0.105	0.118	0.084	0.121
P-5a	0.054	0.054	0.044	0.049
QP-1b	0.056	0.074	0.043	0.066
P-5b	0.045	0.057	0.043	0.044

TABLE 4. Closest wall-normal distance Δ_p of a trajectory of a particle with $a = 0.012$ and $\varrho = 1.023$ on its attractor.

other is repelling. This interpretation is confirmed by the experimental result: We find an attracting limit cycle near one of the closed streamlines and the absence of such limit cycle near the other closed streamline (where a repelling limit cycle is expected). The slow attraction of the particle to the limit cycle suggests that this limit cycle is indeed created by inertia, because the finite-size effect predicts a rapid attraction to a quasi-periodic attractor (for density-matched particles with $a = 0.012$, see $a = 0.011$ and $a = 0.025$ in table 3). The initial phase of the evolution of a particle with $a = 0.012$ and $\varrho = 1.023$ is equivalent to that of a nearly density-matched particle and can be explained by the particle–boundary interaction, and the particle thus has the tendency to approach a quasi-periodic orbit. The weakly attracting/repelling limit cycles near the closed streamlines due to buoyancy and inertia dominate the long-term behaviour by slowly attracting the particle to the stable limit cycle near one of the closed streamlines, while repelling the particle from the unstable limit cycle near the other closed streamline. However, this particle is ultimately stabilised on a quasi-periodic orbit by the particle–boundary interaction. This interpretation is also supported by observing that the distance of the quasi-periodic orbit (table 4) from the moving wall for a weakly inertial particle (figure 27b) is comparable to that for a nearly density-matched particle with a similar size ($a = 0.011$) shown in figure 13(b). A similar behaviour was found using the model of Romanò *et al.* (2019a) for $\Gamma = 1.7$ (unpublished). The same type of asymmetry should also apply to the period-five attractors. But the period-five KAM tori are too slender to be able to detect a notable difference among the two attractors.

The dynamics of attraction to the inertia-induced limit cycle P1-a for $a = 0.012$ ($a_p = 0.50$ mm) and $\varrho = 1.023$ near the cell boundary at $z = -\lambda/4$ is shown in figure 28. The inertial rate of attraction $\bar{\sigma} = 0.31$ is ~ 4 times smaller than the attraction rate to the quasi-periodic orbit for the nearly density-matched particle with $a = 0.011$ and $\varrho = 1.0001$, and more than ten times smaller than the attraction rates for larger nearly density-matched particles (table 3). This difference is remarkable in view of the attraction rates of the nearly neutrally buoyant particles being hampered by the initial flow transient.

As a final consideration, a weak perturbation by buoyancy ($Fr^{-2} \to 0$) in the presence of inertia would not change the character (inertially attracting/repelling) of both limit cycles. The asymmetry introduced by weak buoyancy would only slightly change the attraction rates. If, however, buoyancy exceeds a critical value such that $Fr^{-2} > Fr_c^{-2}$, the asymmetry it induces apparently changes the sign of the attraction rate of one limit cycles such that one of the two limit cycles in the generic convection cell is attracting and the other repelling.

5.2. *Case $a = 0.012$, $\varrho = 1.045$*

A particle of similar size ($a = 0.012$, $a_p = 0.48$ mm), but slightly heavier ($\varrho = 1.045$), is found to settle either on a periodic orbit, on a quasi-periodic orbit, or on one of two
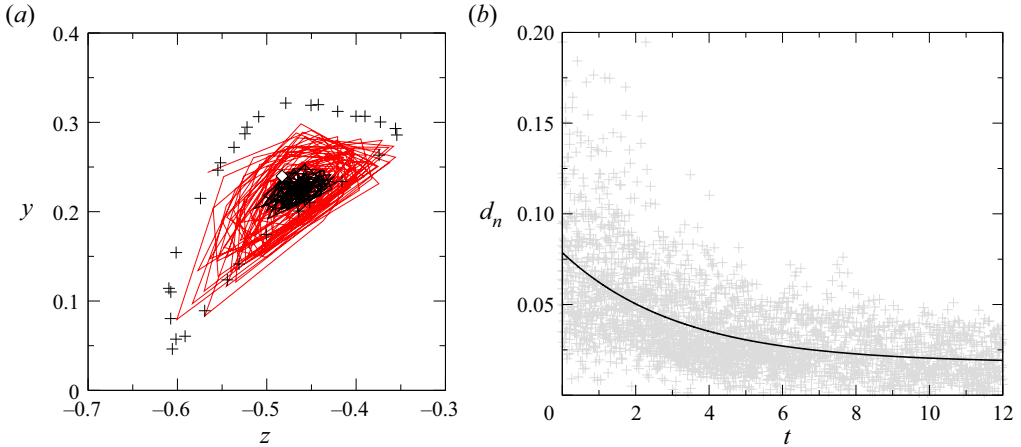
FIGURE 28. (*a*) Poincaré section on $x = 0$ of the trajectory of a single particle (red lines) with $a = 0.012$ and $\varrho = 1.023$ approaching the limit cycle P1-a. The final phase of the evolution is shown by black lines. Pluses indicate the largest numerically reconstructible KAM torus and the diamond marks the closed streamline. (*b*) The distance function d_n for ten realisations (+). A fit of the data according to (4.2) (full line) yields the attraction rate $\bar{\sigma} = 0.31 \pm 0.04$.

period-five orbits. Figure 29 shows the three-dimensional view and the Poincaré section on $y = 0$. The behaviour is similar to that of the particle with $a = 0.012$ ($a_p = 0.50$ mm) and $\varrho = 1.023$. In 13 out of 31 realisations of the experiment the particle was attracted to the period-one limit cycle P-1a (red, left side in figure 29*b*) inside of the main KAM torus near the cell boundary at $z = -\lambda/4$. From these 13 trajectories we find the attraction rate $\bar{\sigma}(a = 0.012, \varrho = 1.045) = 0.49 \pm 0.03$ (figure 30) which is larger than the one for the previous case with only approximately half the density mismatch and $\bar{\sigma}(a = 0.012, \varrho = 1.023) = 0.31 \pm 0.04$.

As for the previous case, two period-five attractors P-5a,b (blue) are present for $a = 0.012$, $\varrho = 1.045$. However, the period-five attractor P-5b near the toroidal attractor QP-1b (red, near $z = \lambda/4$) appears less sharp than the period-five attractor P-5a (blue, near $z = -\lambda/4$) near the period-one limit cycle P-1a. This is interpreted as another consequence of the point-symmetry-breaking effect due to buoyancy discussed above and clearly exhibited by the attractors associated with the period-one KAM tori.

5.3. *Case $a = 0.013$, $\varrho = 1.060$*

Further increasing the particle density to $\varrho = 1.06$, but also slightly increasing the particle size to $a = 0.013$ ($a_p = 0.53$ mm), we find a similar behaviour (figure 31) as for the previously considered particles with smaller density mismatch. We find a period-one (P-1a, red) and a quasi-periodic attractor (QP-1b, red), as well as two period-five attractors (P-5a,b, blue). As expected the attraction rate $\bar{\sigma} = 0.74 \pm 0.06$ to the periodic attractor P1-a (figure 32) is larger than the one for the particles with the smaller density mismatch.

Different from the previous cases, however, we also find a period-four attractor P-4a (black) near $z = -\lambda/2$ which is located between the period-five attractor and the stable limit cycle of period one. Since a period-four KAM torus was not identified in the numerical streamline topology, the period-four attractor is probably caused by inertia in combination with buoyancy. This interpretation is also supported by the observation that the trajectories on the period-four orbit remain distant from the moving boundaries
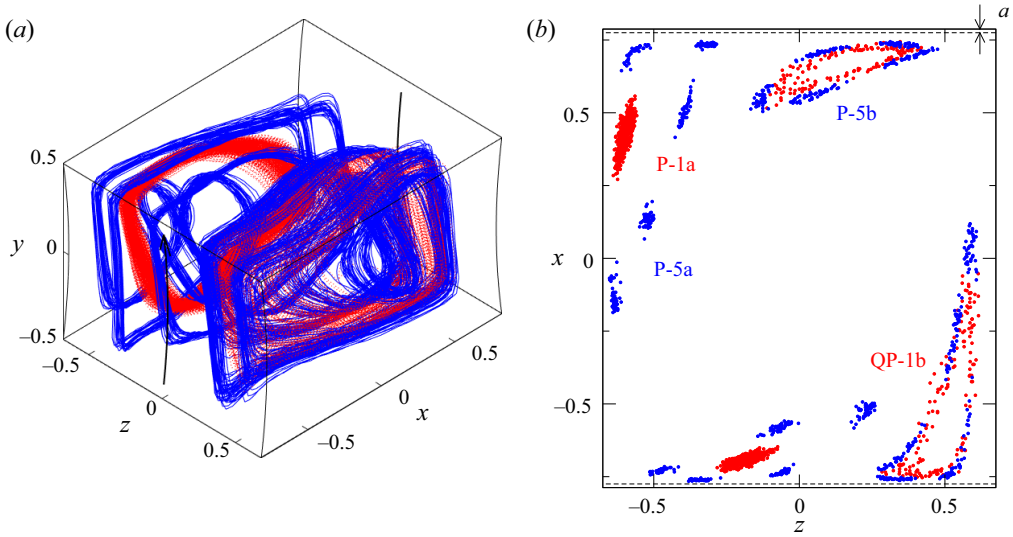
FIGURE 29. Thirty-one trajectories of a single particle with $a = 0.012$ ($a_p = 0.48$ mm) and $\varrho = 1.045$. The trajectories were recorded during $t \in [500, 600]$ s. $T = 23.7\,^\circ$C. (*a*) Three-dimensional view of the trajectories. (*b*) Poincaré section on $y = 0$.
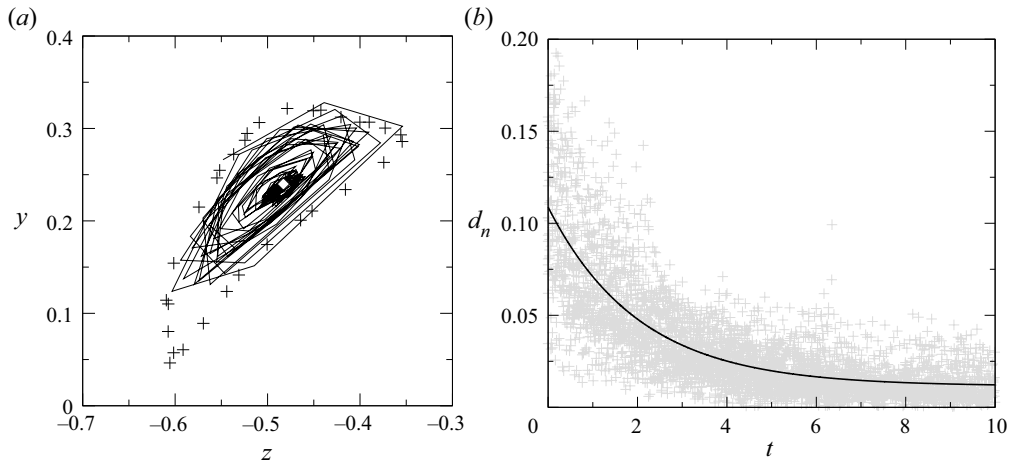

FIGURE 30. (*a*) Poincaré section on $x = 0$ of a single-particle trajectory for $a = 0.012$ ($a_p = 0.48$ mm) and $\varrho = 1.045$ being attracted to the period-one limit cycle P1-a (points connected by lines) in comparison to the largest reconstructible KAM torus (pluses). (*b*) Distance function d_n of 13 realisations (+) and fit $d(t)$ (full line) yielding $\bar{\sigma} = 0.49 \pm 0.03$.

(table 5) such that the finite-particle-size effect near the moving boundaries cannot be responsible for this dissipative structure.

5.4. *Light particle with $a = 0.012$, $\varrho = 0.94$*

To investigate the behaviour of light particles we consider a particle with $a = 0.012$ ($a_p = 0.5$ mm) and $\varrho = 0.94$. The magnitude ($\varrho - 1$) of the density mismatch is the same as
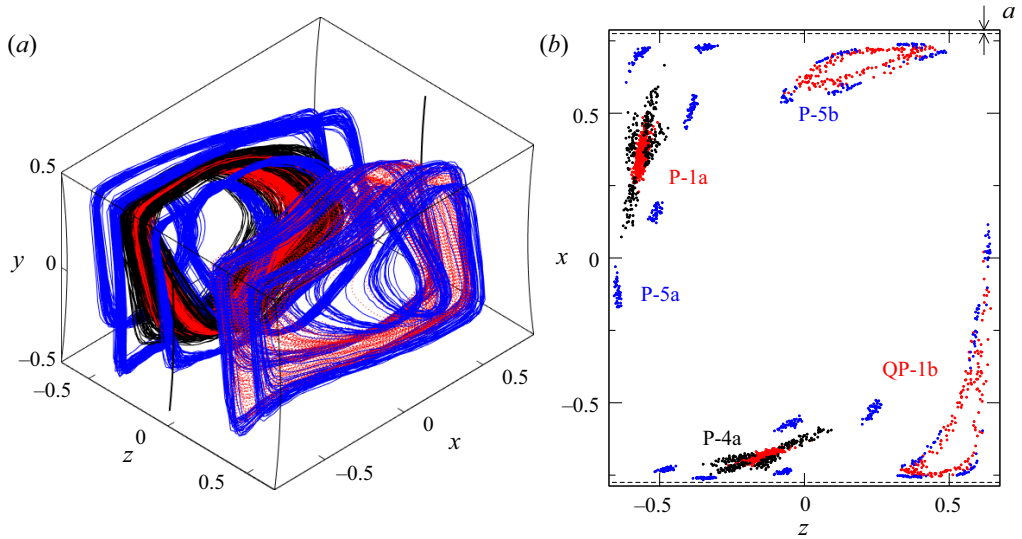
FIGURE 31. Superposition of 33 particle trajectories for $a = 0.013$ ($a_p = 0.53$ mm) and $\varrho = 1.06$. Trajectories have been measured starting 5 min after $Re = 400$ has been reached. $T = 24.5\,^{\circ}$C. (*a*) Three-dimensional view. (*b*) Poincaré section on $y = 0$. The different attractors are colour coded.
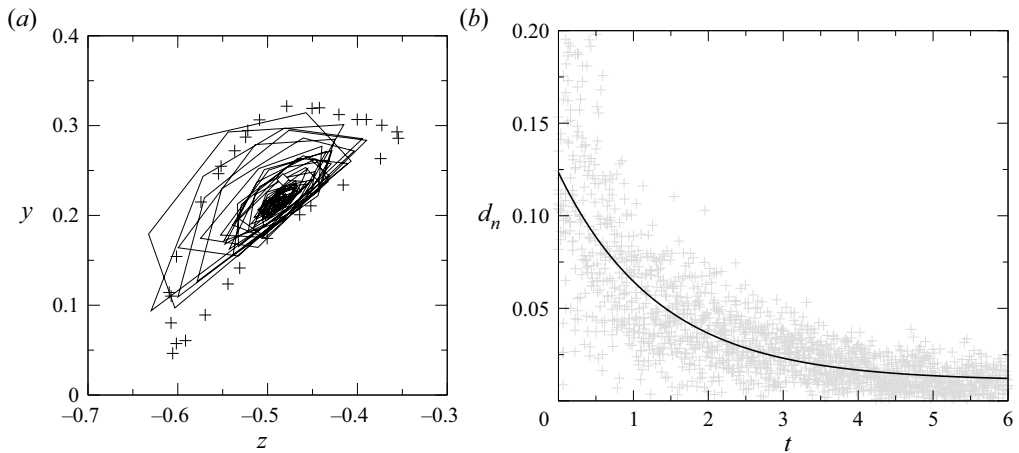

FIGURE 32. (*a*) Poincaré section on $x = 0$ of a single trajectory approaching the period-one limit cycle P-1a for a particle with $a_p = 0.53$ mm and $\varrho = 1.06$ (lines) and largest reconstructible KAM torus (+). (*b*) Distance function d_n for 9 realisations (+) and fit $d(t)$ (full line) yielding the slope $\bar{\sigma} = 0.74 \pm 0.06$ for the attraction rate to the limit cycle.

for the previous particle, but it has a different sign. Trajectories and Poincaré sections are shown in figure 33. As expected from the symmetries of the system, reversing the buoyancy force, the attractors for $\varrho = 0.94$ are point symmetric to those for $\varrho = 1.06$. This can be seen by comparing figure 33(*b*) with figure 31(*b*). The attraction rate $\bar{\sigma} = 0.72 \pm 0.08$ (obtained from figure 34) for the light particle with $\varrho = 0.94$ to the period-one

Attractor	$\Delta_p^{y=0.5}$	$\Delta_p^{y=-0.5}$	$\Delta_p^{x=-\Gamma/2}$	$\Delta_p^{x=\Gamma/2}$
P-1a	0.099	0.126	0.084	0.160
P-4a	0.081	0.098	0.065	0.103
P-5a	0.050	0.054	0.035	0.062
QP-1b	0.068	0.066	0.042	0.067
P-5b	0.056	0.056	0.040	0.058

TABLE 5. Closest wall-normal distances Δ_p of particle trajectories on their attractors for $a = 0.013$ ($a_p = 0.53$ mm) and $\varrho = 1.060$.
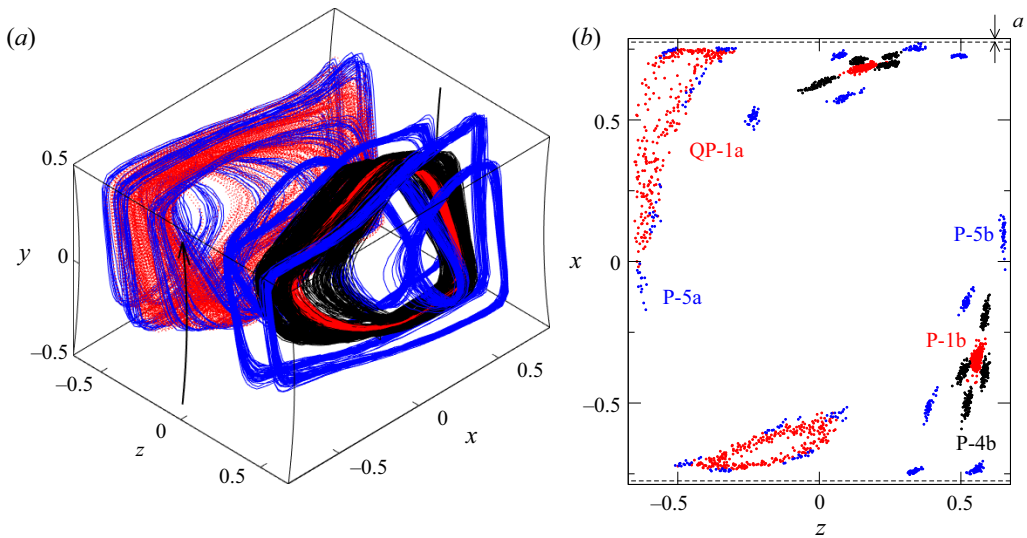

FIGURE 33. Thirty-seven trajectories of individual particles with $a = 0.012$ ($a_p = 0.50$ mm) and $\varrho = 0.94$. Trajectories were recorded during $t \in [400, 500]$ s. $T = 25.5\,^{\circ}\text{C}$. (*a*) Three-dimensional view. (*b*) Poincaré section on $y = 0$. The attractors are distinguished by colour and labels.

limit cycle P-1b (red in figure 33) nearly equals the one (P-1a) for the heavy particle with $\varrho = 1.06$ for which $\bar{\sigma} = 0.74 \pm 0.06$ (figure 32).

5.5. *Attraction rates to the period-one limit cycle*

Figure 35 shows the rate of attraction to the period-one limit cycle as function of the particle-to-fluid density ratio ϱ for particles of nearly the same size with particle radii $a = 0.012$ and $a = 0.013$, i.e. particles with $a_p \in [0.48, 0.53]$ mm. Within the range of ϱ considered the attraction rate increases linearly with the absolute value of the density mismatch $|\varrho - 1|$. This dependence is in agreement with (5.1) in which both inertia and buoyancy terms scale with $|\varrho - 1|$ for constant Stokes number St. Numerical simulations of the particle motion in a rectangular cavity with $Re = 400$, $\Gamma = 1.7$ and zero gravity by Romanò *et al.* (2019*a*) yielded attraction rates due to inertia alone (bullets and the squares in figure 4(*c*) of Romanò *et al.* 2019*a*) with slopes $\partial_\varrho \sigma (a = 0.01) \approx 2$ and $\partial_\varrho \sigma (a = 0.02) \approx 8$ which are of the same order of magnitude as our present measurements which
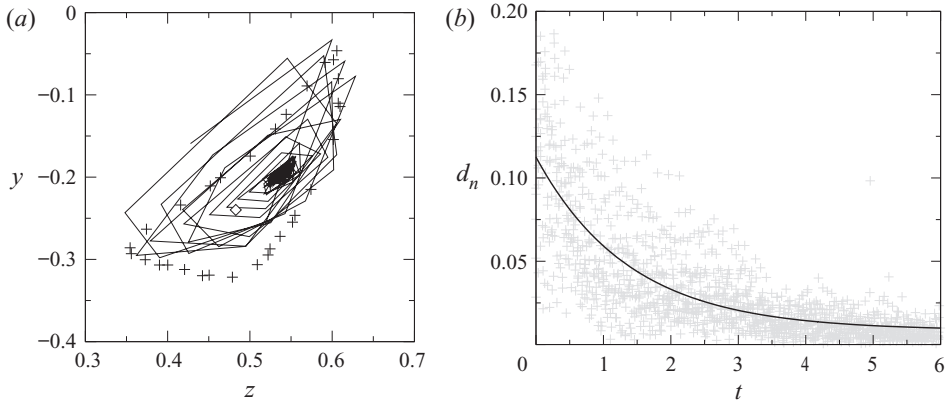
FIGURE 34. (*a*) Poincaré section for a single representative trajectory approaching the period-one limit cycle P-1b for a particle with $a = 0.012$ ($a_p = 0.50$ mm) and $\varrho = 0.94$ (points connected by lines) and largest reconstructible KAM torus (pluses). (*b*) Distance function d_n for nine measurements (+) and fit $d(t)$ (full line) according to (4.2) yielding the attraction rate to the period-one limit cycle $\bar{\sigma} = 0.72 \pm 0.08$.
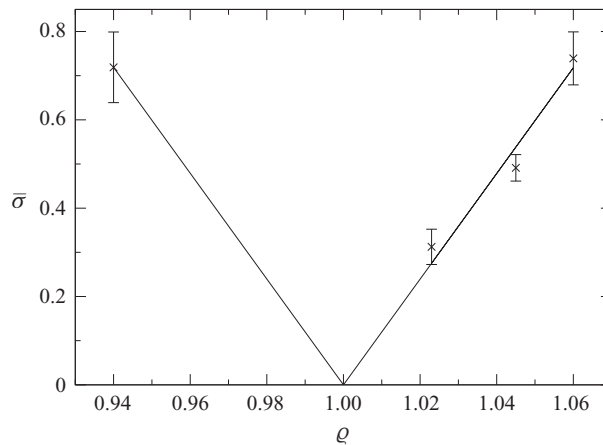

FIGURE 35. Mean rate of attraction $\bar{\sigma}$ to the period-one limit cycle (crosses) as a function of the density ratio $\varrho = 0.94$, 1.023, 1.045 and 1.06 for particles of nearly the same size with particle radii $a = 0.012$ and $a = 0.013$, i.e. $a_p \in [0.48, 0.53]$ mm. The full lines represent linear fits with slopes $|\partial\sigma/\partial\varrho| = 12$.

yield $|\partial\sigma/\partial\varrho| = 12 \pm 1$ for $a = 0.012$ and $a = 0.013$. The remaining deviations may be caused by the different aspect ratio, the different wall curvatures and the stabilising effect of buoyancy in our experiments. In the numerical simulations for $\Gamma = 1.7$ and straight moving walls KAM tori of higher periodicity are absent.

5.6. *Case $a = 0.012$, $\varrho = 1.08$*

For even heavier particles with density ratio $\varrho = 1.08$, keeping the particle radius almost the same as before at $a = 0.012$ ($a_p = 0.48$ mm), the period-five attractor in the right half of the convection cell (near $z = \lambda/4$) vanishes completely (figure 36), while it persists on the left side (P-5a, blue, near the cell boundary $z = -\lambda/4$). This is consistent with the previous interpretation that one inertia-induced limit cycle is stabilised by
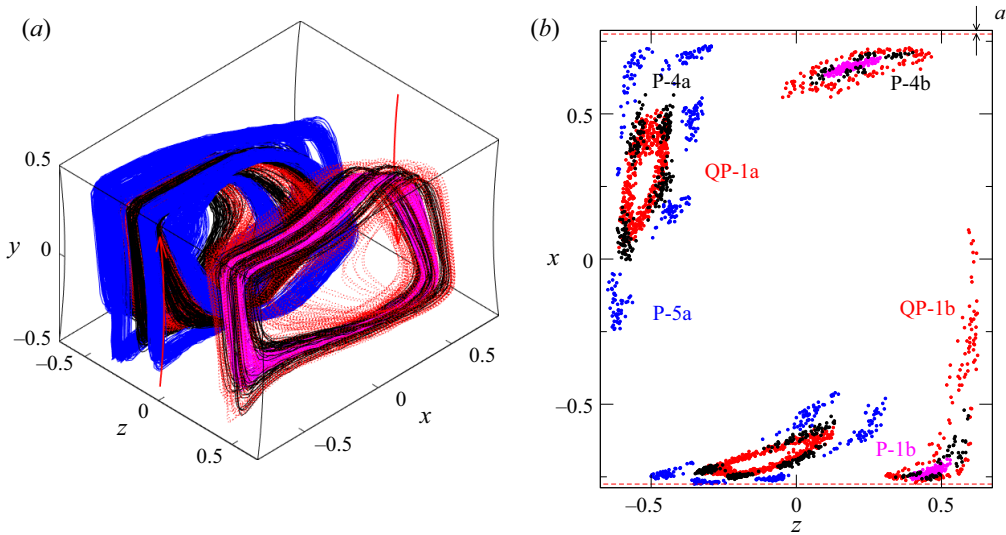
FIGURE 36. Forty trajectories of particles with $a = 0.012$ ($a_p = 0.48$ mm) and $\varrho = 1.08$. The trajectories were recorded 5 min after $Re = 400$ was reached. $T = 26.4\,°\mathrm{C}$. (*a*) Three-dimensional view. (*b*) Poincaré section on the plane $y = 0$.

buoyancy (near $z = -\lambda/4$), while the other one (near $z = \lambda/4$) is destabilised. Particles being repelled from the unstable limit cycle could be attracted to a nearby slender period-five toroidal attractor created by the particle–boundary interaction. In the present case, however, the inertial–buoyancy destabilisation seems to overcome the stabilisation by particle–boundary interaction and QP-5b is absent.

There are four qualitative changes compared to the case $a = 0.013$ ($a_p = 0.53$ mm) and $\varrho = 1.06$ (figure 31). The first is the transformation of the period-one attractor P-1a near $z = -\lambda/4$ caused by inertia (red in figure 31) to a tubular quasi-periodic attractor QP-1a (red in figure 36). It is surrounded by the period-four attractor P-4a (black) which prevails. The second change is the absence of the period-five attractor near $z = \lambda/4$. The third difference is the creation of a periodic attractor P-1b (magenta) inside of the still existing tubular period-one attractor QP-1b (red) near the cell boundary at $z = \lambda/4$ (right hand side of figure 36*b*). As the fourth difference, the new periodic attractor P-1b is surrounded by a newly created period-4 attractor P-4b (black). Apparently, the stability of the two period-one limit cycles has changed (change of sign of σ) upon increasing the density mismatch $\varrho - 1$: The period-one limit cycle near $z = -\lambda/4$ has become unstable, while the period-one limit cycle near $z = \lambda/4$ has become stable (magenta). The stable quasi-periodic attractor QP-1a (red) which has evolved from the stable limit cycle near $z = -\lambda/4$ must still be due to inertia, because the quasi-periodic orbits on the torus to which the particle is attracted stays further away from the moving walls than the period-five limit cycle P-5a (blue) near $z = -\lambda/4$ and the quasi-periodic attractor QP-1b (due to particle boundary interaction) near $z = \lambda/4$. The minimum distances of these orbits from the boundaries are specified in table 6.

5.7. *Case $a = 0.039$, $\varrho = 1.001$ and $\varrho = 1.006$*

For larger particles buoyancy and inertia effects become even stronger. For particles with $a = 0.039$ ($a_p = 1.58$ mm) and $\varrho = 1.001$ we only find two periodic attractors near the closed streamlines. A three-dimensional view and a Poincaré section are shown

Attractor	$\Delta_p^{y=0.5}$	$\Delta_p^{y=-0.5}$	$\Delta_p^{x=-\Gamma/2}$	$\Delta_p^{x=\Gamma/2}$
QP-1a	0.074	0.130	0.050	0.133
P-4a	0.069	0.126	0.049	0.129
P-5a	0.046	0.026	0.024	0.064
P-1b	0.076	0.115	0.039	0.097
QP-1b	0.041	0.090	0.037	0.074
P-4b	0.057	0.100	0.041	0.084

TABLE 6. Closest wall-normal distance Δ_p of trajectories of particles with $a = 0.012$ ($a_p = 0.48$ mm) and $\varrho = 1.08$ moving on their respective attractors.

in figure 37. Due to the presence of buoyancy, the limit cycles are different, depending on the side of the convection cell in which they arise. This is clearly visible in the projection of the limit cycles to the (x, y) plane shown in figure 37(*c*). The loci of the two limit cycles are not point symmetric with respect to the cell centre $(x, y, z) = (0, 0, 0)$. For a comparison, the same slender KAM tori are shown in black in figure 37(*b*), which were compared in figure 19(*b*) with the trajectory of a particle of the same size but nearly density matched to the fluid with $\varrho = 1.0001$. While the symmetry breaking effect of buoyancy is visible and the trajectory must be affected by inertia, the particles also approach the moving walls up to a distance comparable to their size such that, apart from inertia, also the boundary effect is expected to contribute to the generation of the limit cycles.

The asymmetry between the two limit cycles becomes even stronger when the density ratio is increased to $\varrho = 1.006$. The corresponding trajectories and Poincaré sections are provided in figure 38.

6. Discussion and conclusion

The incompressible flow at $Re = 400$ in a long two-sided lid-driven cavity with cross-sectional aspect ratio $\Gamma = 1.6$ arises in form of steady spatially periodic cells. This cellular flow hosts regular streamlines on KAM tori of period one and period five, surrounded by chaotic streamlines which occupy most of the domain, including a layer along all cavity walls (see also Romanò *et al.* 2017).

Individual spherical particles suspended in the cellular flow whose density does not differ much from that of the fluid are found to be attracted to a variety of limit cycles and quasi-periodic orbits. All attractors for the particle motion found are located in or close to the KAM tori of the unperturbed cellular flow, regardless of the particle's initial condition. If several non-interacting particles were considered, the large part of the domain which is occupied by chaotic streamlines would become depleted of particles. Since the trajectories of the particles considered do not deviate much from the streamlines of the flow in the bulk, the particles will eventually be transported along chaotic streamlines to the vicinity of the moving walls where the motion of the particles becomes restricted owing to their finite size. A particle can then be transferred to the region of KAM tori if these are located within a distance from the walls over which the wall effect on the particle is operative (Hofmann & Kuhlmann 2011; Muldoon & Kuhlmann 2013).

If particle inertia and buoyancy are minimised, in the present experiments by selecting the relative density $\varrho = 1.0001$, and if the particle size is not too small we find the particles to be attracted to either periodic orbits which are located in very close vicinity of the closed streamlines of the flow, or to quasi-periodic orbits which practically coincide
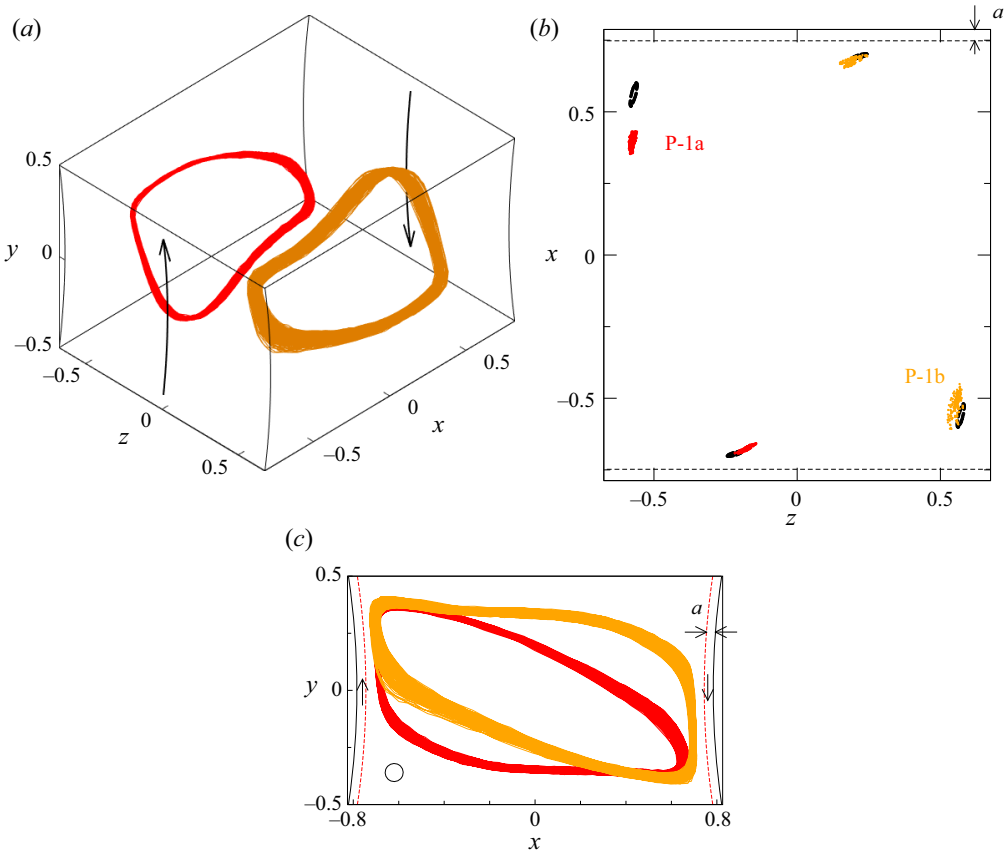
FIGURE 37. Twenty trajectories of a particle with $a = 0.039$ ($a_p = 1.58$ mm) and $\varrho = 1.001$. The trajectories were recorded during $t \in [300, 400]$ s. $T = 25\,°C$. (*a*) Three-dimensional view, (*b*) Poincaré section on the plane $y = 0$ including the contours of two slender KAM tori (black) and (*c*) projection of the trajectories onto the (x, y)-plane.

with a KAM torus of the flow. Since $\varrho = 1.0001$ is very small, the particles nearly move like tracers in the bulk. In this situation the theoretical concept of Hofmann & Kuhlmann (2011) and Romanò *et al.* (2019*b*) for the motion of finite-size particles should be applicable. Our experimental results are, indeed, consistent with this theoretical model which explains the creation of attractors for the particle motion by a particle–boundary interaction that introduces a dissipate effect in the dynamical system governing the particle motion. Particle–boundary interaction can be effective in the present experiments, because the minimum distances of the closed streamlines Δ_ψ inside the KAM tori from the moving walls are of the same order of magnitude as the distance $\Delta = a + \delta$ (*a*: particle radius, δ: thickness of the lubrication layer) over which the finite-size particle–wall effect is operative. For nearly neutral buoyancy we find particle-motion attractors in the representative convection cell which exhibit the same symmetries as the flow field.

The attraction to periodic or quasi-periodic orbits due to the boundary interaction effect is typically very rapid, because the process scales with the turnover time $\tau_1 \approx 0.03 \ll 1$ (non-dimensional viscous time) of the respective orbit (table 3), independent of the density
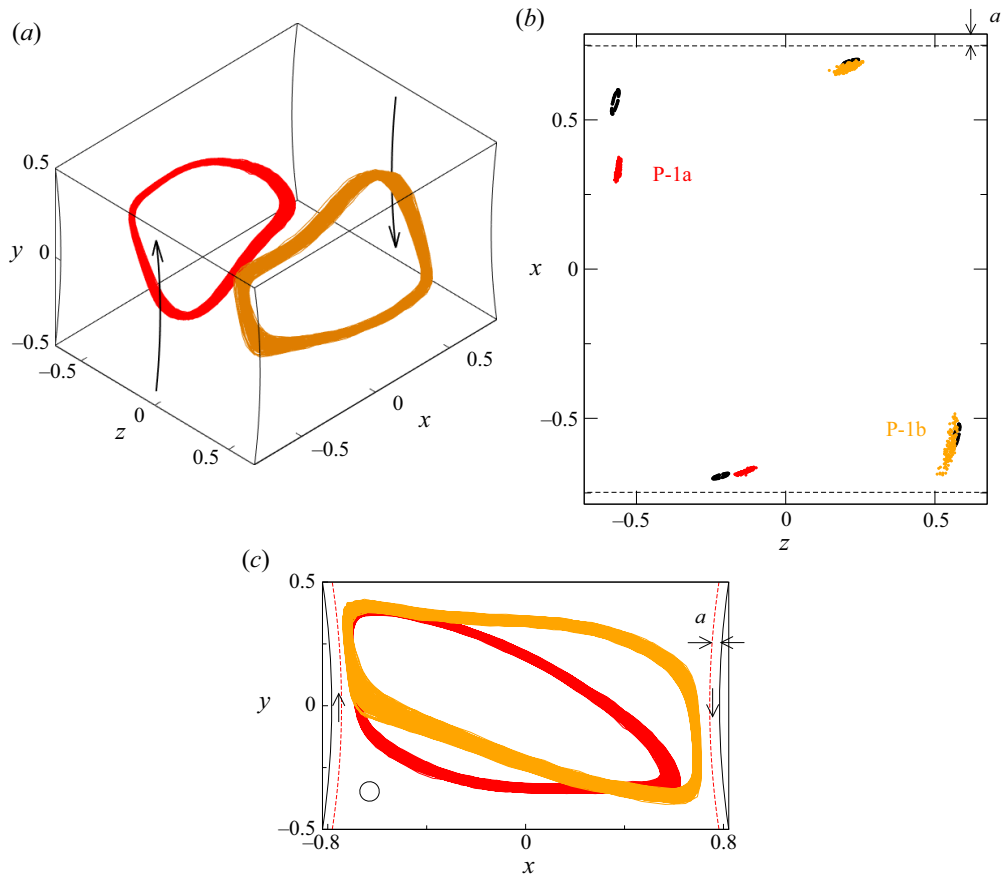
FIGURE 38. Twenty trajectories of a particle with $a = 0.039$ ($a_p = 1.58$ mm) and $\varrho = 1.006$. Trajectories were recorded during $t \in [300, 400]$ s. $T = 28\,^{\circ}$C. (*a*) Three-dimensional view, (*b*) Poincaré section on the plane $y = 0$ including the contours of two slender KAM tori (black) and (*c*) projection of the trajectories onto the (x, y)-plane.

ratio (Kuhlmann *et al.* 2014; Muldoon & Kuhlmann 2016). In contrast, the inertial time scale $\sim |\varrho - 1|^{-1} St^{-1}$ can become very large as $|\varrho - 1| \rightarrow 0$.

　　The attraction rates expected due to the finite-particle-size effect based on the theoretical model of Hofmann & Kuhlmann (2011) and estimated in appendix B is $\sigma = O(20)$. Similarly, the attraction rate obtained numerically by Romanò *et al.* (2019*a*) for a very similar system is $\sigma = O(30)$. This is faster than the dynamics found in our experiments for nearly neutrally buoyant particles for which the mean attraction rate to periodic or quasi-periodic orbits ranges in [1.2, 4.6]. The reason is the most prominent signal for d_n arises during the transient evolution of the flow. Therefore, the measured attraction rates $\bar{\sigma}$ are lower bounds on the attraction rates a particle would experience if it could be initialised in a steady flow. Yet, the focusing of particles via the particle–boundary interaction effect is much faster than the inertial focussing for which the attraction rates can be measured more accurately.

　　When the magnitude of the density mismatch $|\varrho - 1|$ increases, inertia and buoyancy effects gradually become important. It is known that stable or unstable limit cycles due to inertia evolve from the closed streamlines which are equilibrium trajectories for

perfectly advected particles (in the absence of inertia and other forces). Owing to the symmetries of the flow and of the inertia forces both the limit cycles evolving out of each closed streamline of a pair must have the same stability properties. Since both the flow field and the leading-order inertia term are point-symmetric, the removal of the degeneracy of the attraction/repulsion rates to/from the limit cycles is essentially caused by the symmetry-breaking buoyancy forces. In our experiments, we find that the relative strength $\sim Fr^{-2}$ of buoyancy to inertia forces on the particle is so large that even the sign of the attraction/repulsion rate of one limit cycle is changed by buoyancy, rendering one limit cycle of the inertial particle stable and the other unstable. The particle motion near the unstable limit cycle can, however, be stabilised on a quasi-periodic orbit surrounding the unstable limit cycle, where the quasi-periodic orbit is created by the particle–wall effect, similar as for nearly density-matched particles. For even larger density mismatch the inertia–buoyancy-unstable limit cycle inside of the boundary-induced quasi-periodic attractor is found to stabilise again. This observation suggests that a new unstable inertia–buoyant quasi-periodic attractor has been created between the stable inertia–buoyant limit cycle and the stable boundary-induced quasi-periodic attractor. Apart from attractors which exhibit the same periodicity as the underlying KAM tori, we also found inertia–buoyancy-induced attractors which exhibit different periodicities, e.g. period four.

The results obtained confirm the predictions of the particle–boundary interaction model of Hofmann & Kuhlmann (2011) according to which attractors for the motion of particles with a suitable finite size are created, if inertia and buoyancy are sufficiently weak (for cavity flow, see Kuhlmann *et al.* 2016; Romanò *et al.* 2019*a*). For dilute suspensions the attractors can be populated by several or even many finite-size particles. Such PAS have been observed in thermocapillary flows (Schwabe *et al.* 2007; Toyama *et al.* 2017; Watanabe *et al.* 2018; Oba *et al.* 2019). The present experimental results have shown that the transfer of particles to attractors by the finite-size boundary interaction is a more general concept and can lead to finite-size coherent structures (Romanò *et al.* 2019*b*). For the present cm size flow and particles in the mm range the restrictions on the density matching are quite severe due to the large buoyancy forces. Buoyancy becomes less important for particles in millimetric thermocapillary flow, and even less in micrometre-scale flows (Orlishausen *et al.* 2017). If, furthermore, the particle size *a* is small, FSCS can be expected to play an important role in incompressible multiphase micro-flows which are often laminar and thus can exhibit KAM structures. The same mechanism may also help explain the preferential orbits of particles in the classical lid-driven cubic cavity observed by Tsorng *et al.* (2006) and Tsorng *et al.* (2008) which have been lacking a plausible explanation as yet.

A proper numerical treatment of the phenomena measured would be desirable. First results for driven-cavity flows are due to Kuhlmann *et al.* (2016) and Romanò *et al.* (2019*a*). Since fully resolving three-dimensional simulations, taking into account all length scales down to the thickness of the lubrication film between particle and boundary, are extremely expensive computationally (for a two-dimensional flow, see Romanò & Kuhlmann 2017*a*), accurate models improving the elementary model of Hofmann & Kuhlmann (2011) must be developed. For small particle Reynolds numbers such model could be based on the asymptotic theory of Brenner (1961) as already applied by Breugem (2010) and Romanò *et al.* (2019*a*). While this approach may be useful for plane boundaries, it is not directly applicable to the particle motion near the singular edges of the cavity where the stationary and the moving wall meets. But regardless of the problem associated with the particle motion near the singular edge and independent of the boundary effect on the particle

motion, the stability of inertia-induced particle limit cycles and quasi-periodic orbits and its dependence on buoyancy would be an interesting subject of future investigations.

Acknowledgements

Declaration of interests

The authors report no conflict of interest.

Appendix A. Particle tracking

Based on the pinhole camera model (Zhang 2000), and considering homogeneous coordinate systems, the sensor-plane coordinates $x_S^{(i)}$ (of the ith camera) and the world coordinates $X_W(t)$ are related by

$$
s \begin{bmatrix} x_S^{(i)}(t) \\ y_S^{(i)}(t) \\ 1 \end{bmatrix} = \boldsymbol{K}^{(i)} \cdot \begin{bmatrix} \boldsymbol{R}^{(i)} & \boldsymbol{t}^{(i)} \end{bmatrix} \cdot \begin{bmatrix} X_W(t) \\ Y_W(t) \\ Z_W(t) \\ 1 \end{bmatrix},
\tag{A 1}
$$

where s is a scale factor, $\boldsymbol{R}^{(i)}$ and $\boldsymbol{t}^{(i)}$ are, respectively, the extrinsic 3×3 rotation and 3×1 translation matrices which define the rigid body transformation between the world and camera coordinates. The matrix

$$
\boldsymbol{K}^{(i)} = \begin{bmatrix} f_l^{(i)} & 0 & c_x^{(i)} \\ 0 & f_l^{(i)} & c_y^{(i)} \\ 0 & 0 & 1 \end{bmatrix},
\tag{A 2}
$$

is the 3×3 camera intrinsic matrix, where $(c_x^{(i)}, c_y^{(i)})$ and $f_l^{(i)}$ are the principal point and the focal length of the camera lens, respectively.

The nine elements of the extrinsic matrix and the three unknowns in the intrinsic matrix can be obtained from the camera calibration process described in Zhang (2000). To that end we captured 12 images per camera of a planar checkerboard pattern in air under different three-dimensional orientations. After the calibration process, the coordinates of the centre of each camera can be determined in world coordinates by

$$
\boldsymbol{C}^{(i)} = -\left[\boldsymbol{R}^{(i)}\right]^{-1} \cdot \boldsymbol{t}^{(i)}.
\tag{A 3}
$$

Since the particle is immersed in oil, the cameras are placed in air, and both fluids are separated by a thick Plexiglas lid, the refraction of the optical ray due to the different indices of refraction needs to be taken into account for the air–Plexiglas and Plexiglas–oil interfaces. Therefore, the position of the particle centroid is determined by ray tracing based on Snell's law (Yamashita *et al.* 2008; Pedersen *et al.* 2018). For each camera, the refracted optical ray from the object point P to the camera-plane centre point $\boldsymbol{C}^{(i)}$ intersects with the air–Plexiglas and Plexiglas–oil interfaces at points $\boldsymbol{P}_1^{(i)}$ and $\boldsymbol{P}_2^{(i)}$, respectively. The direction vectors of the optical rays in air, Plexiglas and oil are, respectively, $\boldsymbol{v}_1^{(i)}$, $\boldsymbol{v}_2^{(i)}$ and $\boldsymbol{v}_3^{(i)}$. The geometry is shown in figure 39.
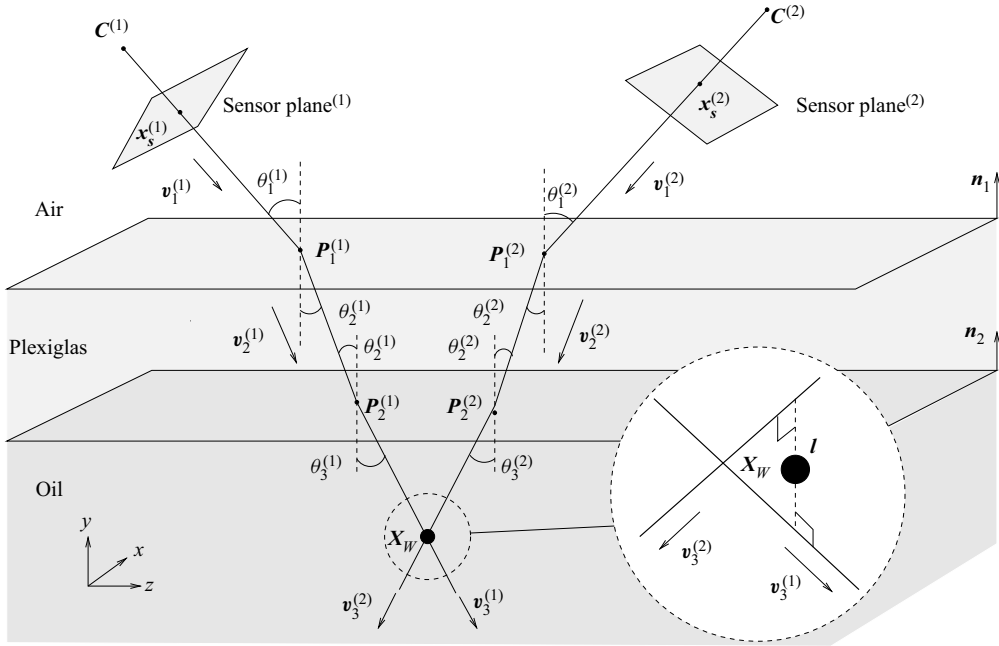
FIGURE 39. For each camera ($i = 1, 2$) $C^{(i)}$ is the camera centre, $P^{(i)}$ is the projection of the point on the sensor and $v_n^{(i)}$ ($n \in [1, 2, 3]$) is the direction vector of the light ray in air, Plexiglas and oil, respectively; X_W is the particle position in world coordinates and l is the line segment perpendicular to both light rays.

Once the sensor coordinates have been determined for each camera by the image processing described in § 2.2, the optical rays in air $r_1^{(i)}$ can be expressed as

$$r_1^{(i)} = C^{(i)} + \alpha^{(i)} v_1^{(i)}, \tag{A 4a}$$

where $\alpha^{(i)}$ is a free parameter. The direction vector $v_1^{(i)}$ can be obtained from the calibrated intrinsic and extrinsic matrix

$$v_1^{(i)} = \left[R^{(i)} \right]^{-1} \cdot \left[K^{(i)} \right]^{-1} \cdot \begin{bmatrix} x_S^{(i)}(t) \\ y_S^{(i)}(t) \\ 1 \end{bmatrix}. \tag{A 4b}$$

The refraction on an air–Plexiglas interface is described by the direction vectors $v_1^{(i)}$ and $v_2^{(i)}$ of the incident and refracted ray, respectively, and the corresponding angles of incidence and refraction $\theta_1^{(i)}$ and $\theta_2^{(i)}$, respectively. The cosine of $\theta_1^{(i)}$ can be expressed as

$$\cos \theta_1^{(i)} = -\frac{n_1 \cdot v_1^{(i)}}{|v_1^{(i)}|}, \tag{A 5}$$

while, based on Snell's law,

$$\cos \theta_2^{(i)} = \sqrt{1 - \left(\frac{n_1}{n_2}\right)^2 (1 - \cos^2 \theta_1^{(i)})}, \tag{A 6a}$$

where $\boldsymbol{n}_1$ is the unit normal vector of the air–Plexiglas interface, and $n_1 = 1$ and $n_2 = 1.49$ are indices of refraction of air and Plexiglas, respectively. The corresponding direction vector of the refracted ray $\boldsymbol{v}_2^{(i)}$ can then be expressed as

$$\boldsymbol{v}_2^{(i)} = \frac{n_1}{n_2}\boldsymbol{v}_1^{(i)} + \left(\frac{n_1}{n_2}\cos\theta_1^{(i)} - \cos\theta_2^{(i)}\right)\boldsymbol{n}_1. \tag{A 6b}$$

Next, in order to determine the optical ray in Plexiglas $\boldsymbol{r}_2^{(i)}$, one needs to know the intersection point $\boldsymbol{P}_1$ between the optical ray and the air–Plexiglas interface which can be described as

$$\boldsymbol{P}_1^{(i)} = \boldsymbol{C}^{(i)} + \alpha_c^{(i)}\boldsymbol{v}_1^{(i)}, \tag{A 7a}$$

where the unknown constant $\alpha_c^{(i)}$ must be determined. Since $\boldsymbol{P}_1$ is a point on the interface, any point $\boldsymbol{P}_{AG}$ on the same plane must satisfy

$$(\boldsymbol{P}_1^{(i)} - \boldsymbol{P}_{AG}) \cdot \boldsymbol{n}_1 = 0. \tag{A 7b}$$

Projecting (A 7a) onto $\boldsymbol{n}_1$ yields

$$\alpha_c^{(i)} = \frac{(\boldsymbol{C}^{(i)} - \boldsymbol{P}_{AG}) \cdot \boldsymbol{n}_1}{\boldsymbol{v}_1^{(i)} \cdot \boldsymbol{n}_1}. \tag{A 7c}$$

The optical ray in Plexiglas can then be expressed as

$$\boldsymbol{r}_2^{(i)} = \boldsymbol{P}_1^{(i)} + \beta^{(i)}\boldsymbol{v}_2^{(i)}, \tag{A 8}$$

where $\beta^{(i)}$ is a free parameter.

As for the Plexiglas–oil interface, the refracted angle $\theta_2^{(i)}$ and direction vector of the optical ray in oil can be determined by the same procedure as described above. We obtain

$$\cos\theta_3^{(i)} = \sqrt{1 - \left(\frac{n_2}{n_3}\right)^2 (1 - \cos^2\theta_2^{(i)})}, \tag{A 9a}$$

$$\boldsymbol{v}_3^{(i)} = \frac{n_2}{n_3}\boldsymbol{v}_2^{(i)} + \left(\frac{n_2}{n_3}\cos\theta_2^{(i)} - \cos\theta_3^{(i)}\right)\boldsymbol{n}_2, \tag{A 9b}$$

where $n_3 = 1.40$ is the refractive index of the working liquid (silicone oil) and $\boldsymbol{n}_2$ the unit normal vector of the Plexiglas–oil interface.

The intersection point of the ray with the Plexiglas–oil interface can then be obtained as

$$\boldsymbol{P}_2^{(i)} = \boldsymbol{P}_1^{(i)} + \beta_c^{(i)}\boldsymbol{v}_2^{(i)}, \tag{A 10a}$$

with the constant

$$\beta_c^{(i)} = \frac{(\boldsymbol{P}_1^{(i)} - \boldsymbol{P}_{GO}) \cdot \boldsymbol{n}_2}{\boldsymbol{v}_2^{(i)} \cdot \boldsymbol{n}_2}, \tag{A 10b}$$

where $\boldsymbol{P}_{GO}$ is an arbitrary point on the Plexiglas–oil interface.

Consequently, the optical ray in oil received by each camera can be expressed as

$$\boldsymbol{r}_3^{(i)} = \boldsymbol{P}_2^{(i)} + \gamma^{(i)}\boldsymbol{v}_3^{(i)}, \tag{A 11}$$

where $\gamma^{(i)}$ is a free parameter.

Ideally, the particle's three-dimensional position vector $X_W(t)$ would locate at the intersection point of the two optical rays $r_3^{(1,2)}$. However, due to errors caused by optical distortion, refraction, and image post-processing, $r_3^{(1)}$ and $r_3^{(2)}$ will not exactly intersect, but miss each other within a small distance. The three-dimensional position is, therefore, estimated by finding the centre of the line segment l connecting the two rays $r_3^{(1,2)}$ perpendicularly, as shown in figure 39. Moreover, $|l|$ can be used as a measure of error of X_W. In the present study we have $|l| \leq 0.6$ mm.

Appendix B. Estimate of the attraction rate to a limit cycle

To estimate the attraction rate to periodic orbits caused by the particle–boundary interaction we consider the perturbed twist map used by Hofmann & Kuhlmann (2011) to model the particle focusing. The map describes the evolution of Poincaré points (x_n, y_n) of the trajectory of a particle which is transported on streamlines in the bulk of the flow domain. The Poincaré plane is selected orthogonal to the closed streamline in the point of closest approach of the closed streamline to the boundary (here the moving wall). The fixed point (x^*, y^*) of the map represents the limit cycle.

In the case when the closed streamline of a KAM torus enters the layer on the moving wall which is inaccessible for the particle centroid and if the winding angle of the streamlines on the KAM tori between two returns to the Poincaré plane is $\theta \leq \pi$, θ assumed constant, this map can be written as

$$x_{n+1} = x_n \cos\theta - A \sin\theta, \tag{B 1}$$

where (x_n, A) is the Poincaré point with $y_n = A < 0$, $|A| =$ const. being equal to the penetration depth of the closed streamline into the inaccessible layer. Since the simplified map (B 1) is linear, the convergence is independent of the additive constant $A \sin\theta$, and governed by $d_{n+1} = d_n \cos\theta$, where $d_n = x_n - x^*$ with $(x^*, y^*) = [-A/\tan(\theta/2), A]$ being the fixed point. With the identification $d_n \hat{=} d(t)$ and the time τ between successive returns to the Poincaré plane we can define $\dot{d} := [d(t + \tau) - d(t)]/\tau$ and obtain

$$\dot{d} = \frac{\cos\theta - 1}{\tau} d, \tag{B 2}$$

with the solution $d \sim \exp\{(\cos\theta - 1)t/\tau\}$. Thus, within the model of Hofmann & Kuhlmann (2011), the attraction rate $\sigma = (1 - \cos\theta)/\tau$ depends only on the winding angle θ and the return time (turnover time).

For the case $a = 0.05$ and $\varrho = 1.0001$ (attraction to a limit cycle) we find the mean winding angle $\bar{\theta}(a = 0.050) = 1.22 < \pi$ and the turn-over period $\tau_1 = 0.0328$ (see table 3) which yields $\sigma = 20.0$.

REFERENCES

ALBENSOEDER, S. & KUHLMANN, H. C. 2002 Linear stability of rectangular cavity flows driven by anti-parallel motion of two facing walls. *J. Fluid Mech.* **458**, 153–180.

AREF, H. 1984 Stirring by chaotic advection. *J. Fluid Mech.* **143**, 1–21.

BAJER, K. 1994 Hamiltonian formulation of the equations of streamlines in three-dimensional steady flow. *Chaos, Solitons Fractals* **4**, 895–911.

BLOHM, C. & KUHLMANN, H. C. 2002 The two-sided lid-driven cavity: experiments on stationary and time-dependent flows. *J. Fluid Mech.* **450**, 67–95.

BRENNER, H. 1961 The slow motion of a sphere through a viscous fluid towards a plane surface. *Chem. Engng Sci.* **16**, 242–251.

BREUGEM, W.-P. 2010 A combined soft-sphere collision / immersed boundary method for resolved simulations of particulate flows. In *Proceedings of the ASME 2010 3rd Joint US-European Fluids Engineering Summer Meeting and 8th International Conference on Nanochannels, Microchannels, and Minichannels*, pp. FEDSM–ICNMM2010–30634. ASME.

CHAOUI, M. & FEUILLEBOIS, F. 2003 Creeping flow around a sphere in a shear flow close to a wall. *Q. J. Mech. Appl. Maths* **56**, 381–410.

CUI, Y., RAVNIK, J., HRIBERŠEK, M. & STEINMANN, P. 2020 Towards a unified shear-induced lift model for prolate spheroidal particles moving in arbitrary non-uniform flow. *Computers & Fluids* **196**, 104323.

DONG, J., INTHAVONG, K. & TU, J. 2017 Multiphase flows in biomedical applications. In *Handbook of Multiphase Flow Science and Technology* (ed. G. H. Yeoh), pp. 1–24. Springer.

FISCHER, P. F., LOTTES, J. W. & KERKEMEIER, S. G. 2008 NEK5000 Web Page. Available at: http://nek5000.mcs.anl.gov.

GOTODA, M., TOYAMA, A., ISHIMURA, M., SANO, T., SUZUKI, M., KANEKO, T. & UENO, I. 2019 Experimental study of coherent structures of finite-size particles in thermocapillary liquid bridges. *Phys. Rev. Fluids* **4**, 094301.

HALLER, G. 2015 Lagrangian coherent structures. *Annu. Rev. Fluid Mech.* **47**, 137–162.

HOFMANN, E. & KUHLMANN, H. C. 2011 Particle accumulation on periodic orbits by repeated free surface collisions. *Phys. Fluids* **23**, 0721106.

JEFFERY, G. B. 1915 On the steady rotation of a solid of revolution in a viscous fluid. *Proc. Lond. Math. Soc.* **2**, 327–338.

KARIMI, A., YAZDI, S. & ARDEKANI, A. M. 2013 Hydrodynamic mechanisms of cell and particle trapping in microfluidics. *Biomicrofluidics* **7**, 021501.

KARNIADAKIS, G. E., ISRAELI, M. & ORSZAG, S. A. 1991 High-order splitting methods for the incompressible Navier–Stokes equations. *J. Comput. Phys.* **97**, 414–443.

KUHLMANN, H. C., MUKIN, R. V., SANO, T. & UENO, I. 2014 Structure and dynamics of particle-accumulation in thermocapillary liquid bridges. *Fluid Dyn. Res.* **46**, 041421.

KUHLMANN, H. C. & MULDOON, F. H. 2012 Particle-accumulation structures in periodic free-surface flows: inertia versus surface collisions. *Phys. Rev.* E **85**, 046310.

KUHLMANN, H. C. & MULDOON, F. H. 2013 On the different manifestations of particle accumulation structures (PAS) in thermocapillary flows. *Eur. Phys. J. Special Topics* **219**, 59–69.

KUHLMANN, H. C. & ROMANÒ, F. 2019 The lid-driven cavity. In *Computational Modelling of Bifurcations and Instabilities in Fluid Dynamics* (ed. A. Gelfgat), pp. 233–309. Springer.

KUHLMANN, H. C., ROMANÒ, F., WU, H. & ALBENSOEDER, S. 2016 Particle-motion attractors due to particle-boundary interaction in incompressible steady three-dimensional flows. In *The 20th Australasian Fluid Mechanics Conference* (ed. G. Ivey, T. Zhou, N. Jones & S. Draper), Paper no. 449, p. 102. Australasian Fluid Mechanics Society.

KUHLMANN, H. C., WANSCHURA, M. & RATH, H. J. 1997 Flow in two-sided lid-driven cavities: non-uniqueness, instabilities, and cellular structures. *J. Fluid Mech.* **336**, 267–299.

LA MANTIA, M. 2017 Particle dynamics in wall-bounded thermal counterflow of superfluid helium. *Phys. Fluids* **29**, 065102.

LASHERAS, J. C. & TIO, K.-K. 1994 Dynamics of a small spherical particle in steady two-dimensional vortex flows. *Appl. Mech. Rev.* **47** (6S), S61–S69.

MATSUNAGA, D., MENG, F., ZÖTTL, A., GOLESTANIAN, R. & YEOMANS, J. M. 2017 Focusing and sorting of ellipsoidal magnetic particles in microchannels. *Phys. Rev. Lett.* **119**, 198002.

MAXEY, M. R. & RILEY, J. J. 1983 Equation of motion for a small rigid sphere in a nonuniform flow. *Phys. Fluids* **26**, 883–889.

MUKIN, R. V. & KUHLMANN, H. C. 2013 Topology of hydrothermal waves in liquid bridges and dissipative structures of transported particles. *Phys. Rev.* E **88**, 053016.

MULDOON, F. H. & KUHLMANN, H. C. 2013 Coherent particulate structures by boundary interaction of small particles in confined periodic flows. *Physica* D **253**, 40–65.

MULDOON, F. H. & KUHLMANN, H. C. 2016 Origin of particle accumulation structures in liquid bridges: particle–boundary interactions versus inertia. *Phys. Fluids* **28**, 073305.

NEWHOUSE, S., RUELLE, D. & TAKENS, F. 1978 Occurence of strange axiom A attractors near quasiperiodic flow on t^m, $m \geq 3$. *Commun. Math. Phys.* **64**, 35–40.

OBA, T., TOYAMA, A., HORI, T. & UENO, I. 2019 Experimental study on behaviors of low-Stokes number particles in weakly chaotic structures induced by thermocapillary effect within a closed system with a free surface. *Phys. Rev. Fluids* **4**, 104002.

ORLISHAUSEN, M., BUTZHAMMER, L., SCHLOTBOHM, D., ZAPF, D. & KÖHLER, W. 2017 Particle accumulation and depletion in a microfluidic Marangoni flow. *Soft Matter* **13**, 7053–7060.

OTTINO, J. M. 1989 *The Kinematics of Mixing: Stretching, Chaos, and Transport*. Cambridge University Press.

PEDERSEN, M., BENGTSON, S. H., GADE, R., MADSEN, N. & MOESLUND, T. B. 2018 Camera calibration for underwater 3d reconstruction based on ray tracing using snell's law. In *2018 IEEE/CVF Conference on Computer Vision and Pattern Recognition Workshops (CVPRW)*, pp. 1491–14917. IEEE/Computer Vision Foundation.

ROMANÒ, F., ALBENSOEDER, S. & KUHLMANN, H. C. 2017 Topology of three-dimensional steady cellular flow in a two-sided anti-parallel lid-driven cavity. *J. Fluid Mech.* **826**, 302–334.

ROMANÒ, F., DES BOSCS, P.-E. & KUHLMANN, H. C. 2020 Forces and torques on a sphere moving near a dihedral corner in creeping flow. *Eur. J. Mech.* B/*Fluids* **84**, 110–121.

ROMANÒ, F., HAJISHARIFI, A. & KUHLMANN, H. C. 2017 Cellular flow in a partially filled rotating drum: regular and chaotic advection. *J. Fluid Mech.* **825**, 631–650.

ROMANÒ, F. & KUHLMANN, H. C. 2015 Interaction of a finite-size particle with the moving lid of a cavity. *PAMM* **15** (1), 519–520.

ROMANÒ, F. & KUHLMANN, H. C. 2017a Particle–boundary interaction in a shear-driven cavity flow. *Theor. Comput. Fluid Dyn.* **31**, 427–445.

ROMANÒ, F. & KUHLMANN, H. C. 2017b Smoothed-profile method for momentum and heat transfer in particulate flows. *Intl J. Numer. Meth. Fluids* **83**, 485–512.

ROMANÒ, F. & KUHLMANN, H. C. 2018 Finite-size Lagrangian coherent structures in thermocapillary liquid bridges. *Phys. Rev. Fluids* **3**, 094302.

ROMANÒ, F. & KUHLMANN, H. C. 2019 Finite-size coherent structures in thermocapillary liquid bridges: a review. *Intl J. Microgravity Sci. Appl.* **36**, 360201.

ROMANÒ, F., KUNCHI KANNAN, P. & KUHLMANN, H. C. 2019a Finite-size Lagrangian coherent structures in a two-sided lid-driven cavity. *Phys. Rev. Fluids* **4**, 024302.

ROMANÒ, F., TÜRKBAY, T. & KUHLMANN, H. C. 2020 Lagrangian chaos in steady three-dimensional lid-driven cavity flow. *Chaos* **30**, 073121.

ROMANÒ, F., WU, H. & KUHLMANN, H. C. 2019b A generic mechanism for finite-size coherent particle structures. *Intl J. Multiphase Flow* **111**, 42–52.

SAPSIS, T. & HALLER, G. 2010 Clustering criterion for inertial particles in two-dimensional time-periodic and three-dimensional steady flows. *Chaos* **20**, 017515.

SCHWABE, D., MIZEV, A. I., UDHAYASANKAR, M. & TANAKA, S. 2007 Formation of dynamic particle accumulation structures in oscillatory thermocapillary flow in liquid bridges. *Phys. Fluids* **19**, 072102.

SIEGMANN-HEGERFELD, T. 2010 Wirbelinstabilitäten und Musterbildung in geschlossenen Rechteckbehältern mit tangential bewegten Wänden (in German). PhD thesis, TU Wien.

SIEGMANN-HEGERFELD, T., ALBENSOEDER, S. & KUHLMANN, H. C. 2008 Two- and three-dimensional flows in nearly rectangular cavities driven by collinear motion of two facing walls. *Exp. Fluids* **45**, 781–796.

SIEGMANN-HEGERFELD, T., ALBENSOEDER, S. & KUHLMANN, H. C. 2013 Three-dimensional flow in a lid-driven cavity with width-to-height ratio of 1.6. *Exp. Fluids* **54**, 1526.

SZELISKI, R. 2010 *Computer Vision: Algorithms and Applications*, 1st edn. Springer.

TANAKA, S., KAWAMURA, H., UENO, I. & SCHWABE, D. 2006 Flow structure and dynamic particle accumulation in thermocapillary convection in a liquid bridge. *Phys. Fluids* **18**, 067103.

TONER, M. & IRIMIA, D. 2005 Blood-on-a-chip. *Annu. Rev. Biomed. Engng* **7**, 77–103.

TOYAMA, A., GOTODA, M., KANEKO, T. & UENO, I. 2017 Existence conditions and formation process of second type of spiral loop particle accumulation structure (SL-2 PAS) in half-zone liquid bridge. *Microgravity Sci. Technol.* **29**, 263–274.

TSORNG, S. J., CAPART, H., LAI, J. S. & YOUNG, D. L. 2006 Three-dimensional tracking of the long time trajectories of suspended particles in a lid-driven cavity flow. *Exp. Fluids* **40**, 314–328.

TSORNG, S. J., CAPART, H., LO, D. C., LAI, J. S. & YOUNG, D. L. 2008 Behaviour of macroscopic rigid spheres in lid-driven cavity flow. *Intl J. Multiphase Flow* **34**, 76–101.

WANG, C., JALIKOP, S. V. & HILGENFELDT, S. 2011 Size-sensitive sorting of microparticles through control of flow geometry. *Appl. Phys. Lett.* **99**, 034101.

WANG, B.-F., MA, D.-J., CHEN, C. & SUN, D.-J. 2012 Linear stability analysis of cylindrical Rayleigh–Bénard convection. *J. Fluid Mech.* **711**, 27–39

WATANABE, T., TAKAKUSAGI, T., UENO, I., KAWAMURA, H., NISHINO, K., OHNISHI, M., SAKURAI, M. & MATSUMOTO, S. 2018 Terrestrial and microgravity experiments on onset of oscillatory thermocapillary-driven convection in hanging droplets. *Intl J. Heat Mass Transfer* **123**, 945–956.

WU, H., ROMANÒ, F. & KUHLMANN, H. C. 2017 Attractors for the motion of finite-size particles in a two-sided lid-driven cavity. *PAMM* **17**, 669–670.

YAMASHITA, A., FUJII, A. & KANEKO, T. 2008 Three dimensional measurement of objects in liquid and estimation of refractive index of liquid by using images of water surface with a stereo vision system. In *2008 IEEE International Conference on Robotics and Automation*, pp. 974–979. IEEE.

ZHANG, Z. 2000 A flexible new technique for camera calibration. *IEEE Trans. Pattern Anal. Mach. Intell.* **22** (11), 1330–1334.